J. Fluid Mech. (2004), *vol.* 507, *pp.* 95–142.
DOI: 10.1017/S0022112004008894 Printed in the United Kingdom

Numerical simulation of detonations in mixtures of gases and solid particles

By MILTIADIS V. PAPALEXANDRIS

Département de Mécanique, Université catholique de Louvain, 1348 Louvain-La-Neuve, Belgium
miltos@term.ucl.ac.be

(Received 8 May 2002 and in revised form 6 January 2004)

This article examines the structure and stability of detonations in mixtures of gases and solid particles via direct numerical simulation. Cases with both reactive and inert particles are considered. First, the two-phase flow model is presented and the assumptions that it is based upon are discussed. Steady-wave structures admitted by the model are subsequently analysed. Next, the algorithm employed for the numerical simulations is described. It is a recently developed high-order shock-capturing algorithm for compressible two-phase flows. The accuracy of the algorithm has been verified through a series of code validation and numerical convergence tests, some of which are included in this article. Subsequently, numerical results for both one-dimensional and two-dimensional detonations are presented and discussed. These results show that the mass, momentum and energy transfers between the two phases result in detonation structures that are substantially different from those observed in the corresponding purely gaseous flows. The effect of certain important parameters, such as particle reactivity, particle volume fraction, and particle diameter, are examined in detail. The numerical results predict that increased particle reactivity suppresses the flow instabilities and increases the detonation velocities. It is further predicted that sufficiently high particle volume fractions can cause detonation quenching regardless of particle reactivity.

1. Introduction

The study of detonations has attracted considerable attention over the years because of the need for prevention of accidental explosions, potential applications to hypersonic propulsion systems, and various industrial applications. In the beginning, most efforts were concentrated in the study of purely gaseous detonations. Thus far, many workers have contributed to the analysis of the structure of these flows. As a result, it has become possible to identify the important mechanisms that influence the stability and propagation of such detonations.

Progress in the field of gaseous detonations paved the way for the study of the significantly more complex phenomena that occur in detonations in two-phase mixtures. The motivation for studying two-phase detonations stems from the range of their applicability. Indeed, such phenomena play an important role in applications such as proposed hypersonic propulsion engine concepts (scramjet, pulse detonatation engine, oblique detonation wave engine), deflagration-to-detonation transition (DDT) in explosive granular materials, and others. The addition of particles in detonatable gases introduces interaction mechanisms between the two phases and new temporal and spatial scales. For example, the energy release behind the leading front might

not be monotonic and might extend over a long region. At present, these interaction mechanisms are not well understood.

Besides their applicability, the study of these flows is of great theoretical interest. For example, the derivation of reliable two-phase detonation and DDT models has been the subject of much work over the years. To this day, many questions on this topic remain open and a universally accepted model for such two-phase flows does not exist (see discussion in the next section). On the other hand, the numerical simulation of these flows is also a challenging task, even with simple two-phase flow models, owing to the large number of spatial and temporal scales associated with them. In particular, simulations of multi-dimensional two-phase detonations are scarce.

To date there have been several experimental studies on two-phase detonations with reactive particles (e.g. Veyssiere & Manson 1982; Peraldi & Veyssiere 1986; Veyssiere 1986; Zhang & Gronig 1991*a*, *b*, 1992). Most of these studies were conducted with aluminium or starch particles. However, there is significant disagreement in the measurements of these studies, so that they cannot be considered conclusive. For example, the detonation velocity measurements on starch suspensions by Zhang & Gronig (1991*a*) was up to four times higher than those reported in Peraldi & Veyssiere (1986). In these experiments, the particle volume fraction was the same, but there were differences in the particle diameter and the tube diameter. This implies that two-phase detonations can be very sensitive to the physical parameters involved and to the dimensions of the flow domain.

In contrast, only a few experimental studies with inert particles have been performed. These include the investigations by Laffite & Bouche (1959), Saint-Cloud *et al.* (1976), Mamontov, Mitrofanov & Sabbotin (1980) and Kaufmann *et al.* (1984). These studies suggested that very small particle diameters or sufficiently high mass loadings can result in detonation failure. (Mass loading is defined as the ratio of particle mass to gaseous mass). More recently, Smirnov, Zverev & Tyurnikov (1996) examined computationally and experimentally the initiation of detonations by a shock wave entering a mixture of gas and (inert or reactive) particles.

Along with the experimental studies, there have been efforts toward the numerical simulation of two-phase detonations. Such simulations, however, are time-consuming and difficult to perform because of the complexity of the interaction mechanisms between gas and particles, and the presence of a multitude of temporal and spatial scales. Required resolutions can easily exhaust most of the computational resources that are currently available. Furthermore, precise data for the oxidization and pyrolysis of certain substances of practical interest (e.g. starch) are not available. As a result, relatively few studies have been devoted to the numerical propagation of detonations in dilute mixtures of gases and heavy solid particles. For example, Khaisanov & Veyssiere (1996) and Uphoff, Hanel & Roth (1995) examined the structure of detonations in mixtures of gases and fine aluminium particles. More recently, Veyssiere, Arfi & Khaisanov (1999) presented results for detonations in starch suspensions. These studies, however, were limited to one-dimensional flows and examined very dilute mixtures only (in particular, the volume occupied by the particles was neglected).

These earlier studies have shown that three different modes of propagation are possible. In the first mode, referred to as 'single-front detonation', the leading front is maintained by the heat release of both gaseous and solid-phase reactions. This is the mode with the highest detonation speed. The second mode is the 'pseudo-gas detonation'. In this case, the front is supported by the burning of the gaseous reactants only. Since the energy from the particle burning is released slowly and away from the leading shock, the speeds of pseudo-gas detonations are smaller than those of

single-front detonations. The third mode is the 'double-front detonation'. In this mode, the leading front is again supported by the gaseous reactions only. The burning of the particles occurs behind the gaseous reaction zone and gives rise to a strong secondary pressure wave which might evolve into a discontinuity; see, Khaisanov & Veyssiere (1996), Uphoff *et al.* (1995). However, it is as yet unclear under which conditions and mixture compositions a second discontinuity can be formed; see the relevant discussion in Veyssiere *et al.* (1999). Existence of these three modes of detonation has been observed experimentally by Peraldi & Veyssiere (1986) and Veyssiere (1986).

So far, only a few efforts have been devoted to multi-dimensional simulations of detonations in mixtures of gases and reactive particles. Apparently, only two previous articles on this topic have been published. Saurel (1996) performed numerical studies on detonation waves inside the combustion chamber of a RAM accelerator. He employed a detailed reaction mechanism for mixtures of $H_2/O_2/He$ gases and hydrazine nitrate particles. Those simulations, however, were conducted on coarse grids (of the order of 2000 cells), suggesting that the reaction zone had not been adequately resolved. Eidelman & Yang (1993) examined the evolution of a blast wave in a system consisting of a cloud with a very small particle volume fraction and a ground layer with very high particle volume fractions. In these simulations only the solid particles were reactive (the gaseous components of the mixture were inert).

Numerical results for detonations with inert particles are also scarce. To the author's knowledge, only Loth, Sivier & Baum (1997) have published a systematic study on this subject. They employed a two-step induction mechanism to model the chemical reactions that take place in a dilute stoichiometric H_2/O_2 system, and they performed simulations on a rectangular computational domain with reflecting-wall conditions on the top and bottom boundaries. However, their hydrodynamic model neglects the volume occupied by the particles. This assumption might not be valid always. In fact, numerical results presented in §§ 5 and 6 of this paper show that a particle compaction zone is formed behind the detonation wave. There are cases where the particle volume fraction becomes large and, therefore, non-negligible inside this compaction zone, even though the quiescent mixture ahead of the front is dilute. Examples of such cases include flows that result in detonation quenching.

In this paper, we are concerned with the analysis and numerical study of detonations in dilute mixtures with both reactive and inert particles. Such studies are useful for hazard assessment in multi-phase media. They can also provide validation of proposals for performance improvement of hypersonic propulsion engine concepts by means of the addition of fine metallic particles (Cambier & Bogdanoff 1993). The main objectives of this work are (i) to obtain information on the structural characteristics of the various modes of propagation of two-phase detonations; (ii) to study the role of certain physical parameters, such as particle reactivity, particle volume fraction and particle diameter; and (iii) to identify the conditions that might lead to the establishment of steady detonation waves, as well as the conditions that can lead to detonation quenching. It must be emphasized that our study is not concerned with detonations in mixtures with explosive granular materials, such as HMX. Instead, we consider solid incompressible particles that are at least three orders of magnitude heavier than the gaseous components of the mixture. Further, we consider particles which can react, if at all, only at substantially high temperatures.

As regards simulations for two-phase mixtures with inert particles, it should be mentioned that there are several differences between our study and that conducted by Loth *et al.* (1997). First, the two-phase flow models employed in our study does not make the assumption of negligible particle volume fraction. Secondly, in our

simulations, periodic conditions have been imposed on the top and bottom boundaries instead of reflecting-wall conditions. Finally, there is a difference between the reaction models employed. In particular, we employ a simplified one-step Arrhenius kinetics law instead of a two-step model with induction parameter. These choices of boundary conditions and reaction models were made to facilitate comparisons with published numerical results for purely gaseous detonations, such as those of Bourlioux & Majda (1992), and Papalexandris, Leonard & Dimotakis (2002). Such comparisons have not previously appeared in the literature.

The paper is organized as follows. First, we provide a description of the two-phase flow model that is employed in our study and we discuss the assumptions that this model is based upon. Next, we present an analysis of the steady-wave solutions that are admitted by the flow model. Subsequently, we present a brief description of the numerical method that has been implemented for the simulations. The next part of the paper is concerned with results from the simulations of one-dimensional detonations. The numerical results elucidate the effect of solid particles on the structure of one-dimensional flows, but they also provide insight on basic features that are encountered in multidimensional flows. Grid convergence tests and parametric studies on the role of various physical parameters have also been included. In the last part of the paper, simulations of two-dimensional detonations are presented and analysed. The presentation of the numerical results is accompanied by comparisons with previous numerical and/or experimental studies.

2. Description of the two-phase flow model

For compressible, purely gaseous flows, the Eulerian description of motion has been employed almost exclusively. For flows with particles, we can select either the Eulerian or Langrangian description for the motion of the particles. The Lagrangian description is better suited, and quite often employed, for flows at low Mach numbers. On the other hand, numerical studies show that for particle motion in high-Mach-number flows, the Eulerian description is more efficient (see the discussion in Sivier, Loth & Baum 1996; Saurel & Lemetayer 2001). In the present study, the Eulerian description has been employed for both phases. The description of the two-phase model is given below.

Consider a dilute and monodisperse mixture of gas and heavy solid particles. The gaseous phase consists of two calorifically perfect gases: the reactive species A and the inert species B. These two substances are assumed to have equal specific heats. The species A reacts according to

$$A \longrightarrow B.$$

The solid phase consists of a single substance, C, which is assumed to be completely incompressible. In some cases this substance is considered to be reactive, while in others it is considered to be inert. If C is reactive, it reacts according to the simplified law

$$C \longrightarrow B.$$

The particle number density is assumed to be high enough that the solid particles can be modelled as a continuum. The flows of the two phases are assumed to be inviscid and non-heat-conducting. Viscosity and heat-transfer effects are taken into account only on the surface of the solid particles.

Let ϕ_g, p_g, ρ_g, T_g, $\boldsymbol{u}_g = (u_g, v_g)$, e_g and z denote volume fraction, pressure, density, temperature (normalized by the gas constant), velocity, total specific energy and reactant mass fraction for the gaseous phase, respectively. The gaseous reactant mass fraction z satisfies $0 \leqslant z \leqslant 1$. It equals unity when the gaseous phase consists only of the reactive substance A, and it equals zero when the gaseous phase consists only of the inert substance B. Similarly, let ϕ_s, ρ_s, T_s, $\boldsymbol{u}_s = (u_s, v_s)$, e_s and N_s denote volume fraction, density, temperature, velocity, total specific energy and number density for the solid phase, respectively. The gaseous phase follows the perfect-gas constitutive relation,

$$p_g = \rho_g T_g, \tag{1}$$

where the gas temperature has been normalized by the gas constant.

The partial density, $\tilde{\rho}_g$, and partial pressure, $\tilde{p}_g$, of the gaseous phase are defined as

$$\tilde{\rho}_g = \rho_g \phi_g, \qquad \tilde{p}_g = p_g \phi_g. \tag{2}$$

The total specific energy of the gaseous phase is given by

$$e_g = \frac{p_g}{\rho_g(\gamma - 1)} + \tfrac{1}{2}|\boldsymbol{u}_g|^2 + q_1 z, \tag{3}$$

where γ is the specific-heat ratio (assumed common for both A and B), and q_1 is the heat release from the gaseous reaction.

The volume fractions are related to the particle number density particle via

$$\phi_s = N_s \frac{\pi d_p^3}{6}, \qquad \phi_s + \phi_g = 1, \tag{4}$$

where d_p is the particle diameter. The partial solid density is defined as

$$\tilde{\rho}_s = \rho_s \phi_s. \tag{5}$$

Finally, the expression for the total specific energy of the solid phase is

$$e_s = c_s T_s + \tfrac{1}{2}|\boldsymbol{u}_s|^2 + q_2, \tag{6}$$

where c_s is the specific heat of the solid substance C, and q_2 is the heat release from the burning of the solid particles.

The conservation equations for the gaseous phase are

$$\frac{\partial \tilde{\rho}_g}{\partial t} + \nabla \cdot (\tilde{\rho}_g \boldsymbol{u}_g) = \Gamma, \tag{7a}$$

$$\frac{\partial \tilde{\rho}_g \boldsymbol{u}_g}{\partial t} + \nabla \cdot (\tilde{\rho}_g \boldsymbol{u}_g \boldsymbol{u}_g) + \nabla \tilde{p}_g = \boldsymbol{F} + \Gamma \boldsymbol{u}_s, \tag{7b}$$

$$\frac{\partial \tilde{\rho}_g e_g}{\partial t} + \nabla \cdot (\boldsymbol{u}_g(\tilde{p}_g + \tilde{\rho}_g e_g)) = \boldsymbol{F} \cdot \boldsymbol{u}_s + \Gamma e_s + Q, \tag{7c}$$

$$\frac{\partial \tilde{\rho}_g z}{\partial t} + \nabla \cdot (\tilde{\rho}_g z \boldsymbol{u}_g) = R. \tag{7d}$$

The conservation equations for the solid phase are

$$\frac{\partial \tilde{\rho}_s}{\partial t} + \nabla \cdot (\tilde{\rho}_s \boldsymbol{u}_s) = -\Gamma, \tag{8a}$$

$$\frac{\partial \tilde{\rho}_s \boldsymbol{u}_s}{\partial t} + \nabla \cdot (\tilde{\rho}_s \boldsymbol{u}_s \boldsymbol{u}_s) = -(\boldsymbol{F} + \Gamma \boldsymbol{u}_s), \tag{8b}$$

$$\frac{\partial \tilde{\rho}_s e_s}{\partial t} + \nabla \cdot (\tilde{\rho}_s \boldsymbol{u}_s e_s) = -(\boldsymbol{F} \cdot \boldsymbol{u}_s + \Gamma e_s + Q), \tag{8c}$$

$$\frac{\partial N_s}{\partial t} + \nabla \cdot (N_s \boldsymbol{u}_s) = 0. \tag{8d}$$

Equation (8d) describes the conservation of the number density of the particles. Although not employed here, phenomena such as breakup or coalescence of particles can be modelled with the addition of a suitable source term in (8d).

In mixtures with reactive particles, the solution to (8a) and (8d) is inserted into (4) to compute the spatial distribution of the particle diameter, d_p. For mixtures with inert particles we have $q_2 = 0$, $\Gamma = 0$. Then, it follows (by virtue of the incompressibility assumption of the solid phase) that when the solid particles are inert, (8a) and (8d) become identical.

In the conservation equations above, $\boldsymbol{F}$ is the term that describes the aerodynamic force acting upon the particles. In the present study, this force is approximated by the drag on a sphere moving at constant speed at low Reynolds numbers, i.e.

$$\boldsymbol{F} = 3\,\pi\, c_D\, \mu\, d_p\, (\boldsymbol{u}_s - \boldsymbol{u}_g)\, N_s, \tag{9}$$

where c_D is the drag coefficient, and μ is the viscosity of the gas.

Additionally, Q is the source term that describes the heat transfer between the two phases. We assume steady conduction, so that Q is given by

$$Q = \pi\, \frac{c_p Nu}{Pr}\, \mu\, d_p\, (T_s - T_g)\, N_s. \tag{10}$$

In (10), Pr and Nu are the Prandtl and Nusselt numbers, respectively, while c_p is the specific heat of the gaseous phase under constant pressure. As mentioned above, c_p is assumed to be the same for both gaseous species A and B.

The gaseous reaction is described by a simple one-step Arrhenius kinetics law,

$$R = -\,K_1\, \tilde{\rho}_g\, z\, \exp(-E_a/T_g), \tag{11}$$

where K_1 and E_a are the reaction's pre-exponential factor and activation energy, respectively. On the other hand, the burning of the particles is modelled by the following ignition-type mechanism,

$$\Gamma = \begin{cases} 0, & T_s < T_{ign}, \\ K_2\, \tilde{\rho}_s / d_p^2, & T_s \geqslant T_{ign}, \end{cases} \tag{12}$$

where K_2 is the time constant of the particle burning, and T_{ign} is the ignition temperature beyond which particles begin to react.

An empirical relationship given by Chapman & Cowling (1961) is employed for the calculation of the gas viscosity, μ, as a function of T_g. This relationship is derived for air and in dimensional form reads

$$\mu = 1.71 \times 10^{-5} \left(\frac{T_g}{T_r}\right)^{0.77} (\mathrm{Kg\,s^{-3}}), \tag{13}$$

where $T_r = 273\,\mathrm{K}$. In the present study, it is assumed that the detonatable gas is a H_2/air mixture, with small concentration of H_2, Thus, it is acceptable to employ the above relationship for the purposes of our study. Non-dimensionalization of this relation is performed with respect to the state of the gas in the quiescent (unshocked) region.

The Prandtl number is assumed constant, $Pr = 3/4$, whereas the Nusselt number is given by the following empirical correlation (Knudsen & Katz 1955),

$$Nu = 2 + 0.6\, Pr^{1/3}\, Re^{1/2}, \tag{14}$$

where Re is the Reynolds number of the particles:

$$Re = \rho_g \, |\boldsymbol{u}_s - \boldsymbol{u}_g| \, \frac{d_p}{\mu}. \tag{15}$$

Finally, the following empirical relationship has been used for the drag coefficient c_D (Rowe 1961),

$$c_D = \begin{cases} 1 + 0.15 Re^{0.687}, & Re < 1000, \\ 0.01833 \, Re, & Re \geqslant 1000. \end{cases} \tag{16}$$

Equations (7)–(8) form a hyperbolic system of conservation laws. The source terms of (7) have opposite sign to the source terms of (8) and, therefore, the overall mass, momentum and energy of the system are conserved. With the use of $\tilde{\rho}_g$ and $\tilde{p}_g$, the left-hand sides of (7) take the form of the left-hand side of the classical gasdynamic Euler equations. This implies that coupling between the two phases comes via (4) and the source terms only. As a result, the eigenvalues of (7) are the same as the eigenvalues of the Euler equations. This has a direct implication in the design of algorithms for the numerical solution of the system (7)–(8).

Further insight into the behaviour of the two-phase mixture can be obtained by considering the limit case of thermal and mechanical equilibrium between the two phases, i.e. when $\boldsymbol{u}_g = \boldsymbol{u}_s, T_g = T_s = T$. Inserting these two conditions into the governing system (7)–(8), it is found, after some straightforward algebra, that at equilibrium the mixture behaves as a perfect gas with an effective specific-heat ratio equal to

$$\gamma_{eq} = \frac{c_p \tilde{\rho}_g + c_s \tilde{\rho}_s}{c_v \tilde{\rho}_g + c_s \tilde{\rho}_s}. \tag{17}$$

The speed of sound of the mixture at equilibrium is given by

$$c_{eq}^2 = \gamma_{eq} \frac{\tilde{p}_g}{\tilde{\rho}_g + \tilde{\rho}_s}. \tag{18}$$

It is worth observing that the equilibrium sound-speed satisfies the condition

$$0 < c_{eq} \leqslant c, \tag{19}$$

where c is the frozen speed of sound for the gas, i.e.

$$c = \left(\frac{\partial p_g}{\partial \rho_g} \right)_s^{1/2}, \tag{20}$$

with s being the entropy of the gas. This implies that the equilibrium characteristic speed lies between the extremal characteristics of the system (7)–(8). Further, the equilibrium properties of the mixture are independent of the particle diameter. On the other hand, (18) implies that the equilibrium sound speed monotonically decreases with the particle volume fraction. In general, this is not correct. However, for small and moderate particle concentrations (such as the those considered in the present study) the equilibrium sound speed does drop monotonically with ϕ_s (see Kapila *et al.* 2001).

Two-phase flow models with the same convective structure have been employed by Eidelman & Yang (1986), and Saurel (1996). Other models for high-speed two-phase reacting flows have also been proposed. Examples include the BN model of Baer & Nunziato (1986), the models of Butler & Krier (1986), Powers, Stewart & Krier (1990*a*), Bdzil *et al.* (1999), Saurel & Abgrall (1999), Saurel & Lemetayer (2001) and

others. Simplified two-phase flow models that neglect the volume occupied by the particles have been employed by Miura & Glass (1982), Loth *et al.* (1997) and others.

At this point, it would be useful to list the main assumptions of the model (7)–(8). Further refinement of this model can be achieved by relaxing some of these assumptions.

(i) The solid phase is modelled as a continuum.
(ii) The solid phase is assumed to be completely incompressible.
(iii) The effect of nozzling terms is negligible.
(iv) The model incorporates a simplified reaction model.
(v) The model employs simplified expressions for the momentum exchange and heat transfer between the two phases. The temperature inside the particles is uniform (heat transfer inside the particles is ignored).

The first assumption suggests that the validity of the model might become questionable at very small particle volume fractions. Roughly speaking, the continuum approximation holds as long as the number density of particles is sufficiently high that it becomes impossible to single out individual particles in the mixture. However, earlier studies and comparisons between experiments and numerical results indicate that the continuum approximation can be valid even for very dilute mixtures (see Ishii, Umeda & Yuhi 1989; Uphoff *et al.* 1995 and references therein).

The second assumption implies that the dynamic compaction equation that is included in the flow models (Baer & Nunziato 1986; Bdzil *et al.* 1999; Saurel & Lemetayer 2001), effectively becomes redundant. This equation is a convection equation for the solid density ρ_s, with a source term that is proportional to the difference between the gas pressure and the sum of the solid pressure and (an estimate for) the intergranular stress. This source term is referred to as the 'pressure relaxation' term and describes the microscale forces that act upon the particles. In general, the solid particles are subject to microscale motion in order to achieve pressure equilibrium between the two phases. However, when the solid substance is incompressible, the solid particles become rigid bodies and their microscale motion vanishes.

According to the third assumption, the effects of the nozzling terms are ignored. These terms appear in the momentum and energy equation for each phase and they have the form $p_i \nabla \phi_s$, and $p_i u_i \nabla \phi_s$. In these expressions, p_i and u_i represent interfacial pressure and velocity, respectively, and they are constructed in a non-unique manner. Nozzling terms are non-conservative. As a result, the evolution of gasdynamic discontinuities does not follow the classical jump conditions. Such terms are included in some two-phase models (Baer & Nunziato 1996; Bdzil *et al.* 1999; Saurel & Lemetayer 2001) and are excluded in others (Butler & Krier 1986; Powers *et al.* 1990*a*).

Inclusion of nozzling terms ensures that the dynamic compaction models satisfy the strong form of the second thermodynamic law which states that each individual process that the mixture undergoes should be dissipative. Additionally, in two-phase flow models where both phases are considered compressible, nozzling terms are necessary in order to avoid velocity and pressure evolution from initial conditions of uniform (and equal for both phases) velocity and pressure distributions (see discussion in Saurel & Abgrall 1999). This argument, however, is not directly applicable in the two-phase flow model presented above because this model assumes an incompressible solid phase.

On the other hand, a number of arguments have been provided for excluding these terms from the governing equations. More specifically, Gonthier & Powers (2000)

mention that (i) only the weak form of the second thermodynamic law has to be satisfied (the overall entropy of an isolated mixture has to be non-decreasing in time, (ii) currently there is no microscale justification for either the inclusion or the exclusion of nozzling terms (in other words, it has not yet been verified that these terms describe actual physical phenomena), (iii) the effect of these terms is negligible in high-pressure environments, and (iv) accurate estimates of the interfacial pressure and velocities are quite often unavailable. Additionally, if the initial conditions contain interfaces across which the particle volume fraction is discontinuous, then the nozzling terms become infinite, thus imposing non-physical singularities on the governing equations. In the present study, nozzling terms have been excluded mainly because in high-pressure conditions (such as those encountered in detonation fronts), the role of these terms is expected to diminish; see also the discussion in Bdzil *et al.* (1999). Besides, Gonthier & Powers (2000) reported good agreement between numerical results obtained with their model (that did not take nozzling into account) and experimental DDT data.

As far as the fourth assumption is concerned, we note that the one-step Arrhenius kinetics law is quite often employed in the numerical simulations of reacting flows (see, for example, Papalexandris, Leonard & Dimotakis 1997, and references therein). It can reproduce some important features of detonations. On the other hand, there are some restrictions and limitations in the applicability of this kinetics law because it cannot provide a precise description of the thermochemistry of real-life detonations. For example, it cannot capture certain phenomena associated with initiation (such as chain-branching) or extinction of detonations.

The assumption that momentum exchange between the two phases occurs only via drag is fairly standard in flow models for mixtures of gases and heavy particles. The justification for neglecting the other hydrodynamic forces is the following (Loth *et al.* 1997). Added mass effects are neglected owing to the large density ratio of the two phases. Lift forces are neglected owing to low vorticity (outside contact discontinuities). In fact, recent three-dimensional numerical simulations by Tomboulides & Orzag (2000) show that lift forces in the Reynolds numbers of interest are typically 15 times smaller than drag forces. Additionally, Basset and Faxen forces are neglected because the scales associated with gas velocity gradients are much larger than the particle size (outside discontinuities).

Finally, the assumption regarding temperature uniformity inside the particles is also fairly standard in two-phase flow models. It is justifiable because of the small size of the particles. However, for large particle diameters this assumption might not be valid anymore. In those cases, the approaches of Fan & Sichel (1988) or Gonthier *et al.* (1998) which take into account heat conduction inside particles, can be used.

3. Steady-wave solutions

In this section, we focus on the analysis of the one-dimensional steady-wave structure. More specifically, we derive a set of four ordinary differential equations (o.d.e.s), and four algebraic constraints that describe steady-state solutions (in the frame attached to the leading front) of the two-phase flow model (7)–(8). These equations can then be integrated numerically for the evaluation of the steady-wave profiles. Such analysis provides a valuable method of algorithm validation. It is also useful for gaining a better understanding of the relaxation processes occurring behind the leading front and for identifying the various modes of two-phase detonation that admit a steady-wave structure.

The method that we employ in our analysis is standard. More specifically, we assume that the solution to the flow model (7)–(8) is a steady one-dimensional detonation wave propagating with speed D. Then, the governing equations are written in a coordinate frame attached to the wave, by using the transformation of coordinates $\xi = x - Dt$, and velocities $w_i = u_i - D$, where $i = g, s$. After some straightforward calculations, the conservation equations for the gaseous reactant mass fraction variable, and particle mass, momentum and energy yield

$$\frac{\mathrm{d}\tilde{\rho}_g z w_g}{\mathrm{d}\xi} = R, \tag{21a}$$

$$\frac{\mathrm{d}\tilde{\rho}_s w_s}{\mathrm{d}\xi} = -\Gamma, \tag{21b}$$

$$\frac{\mathrm{d}w_s}{\mathrm{d}\xi} = -\frac{F}{\tilde{\rho}_s w_s}, \tag{21c}$$

$$\frac{\mathrm{d}T_s}{\mathrm{d}\xi} = -\frac{Q}{c_s\,\tilde{\rho}_s\,w_s}, \tag{21d}$$

respectively. For the calculation of the gas flow variables, we can employ the conservation equations for the mixture. In the steady-wave frame of reference, these equations are transformed to algebraic equations. Similarly, (8d) for the conservation of particle number density yields an algebraic equation for the particle diameter because it is source-free. The final result is

$$\tilde{\rho}_g w_g + \tilde{\rho}_s w_s = C_1, \tag{22a}$$

$$\tilde{\rho}_g w_g^2 + \tilde{\rho}_g T_g + \tilde{\rho}_s w_s^2 = C_2, \tag{22b}$$

$$\tilde{\rho}_g w_g (e_g + \tilde{\rho}_g T_g) + \tilde{\rho}_s w_s e_s = C_3, \tag{22c}$$

$$\frac{\tilde{\rho}_s w_s}{d_p^3} = C_4. \tag{22d}$$

The values of the constants C_i, $i = 1, 2, 3, 4$, are evaluated by direct substitution of the initial conditions to the left-hand side of the above equations. The above system is everywhere regular except at points where $\tilde{\rho}_s = 0$ or $w_s = 0$. These singularities can be removed by using the o.d.e.s that describe conservation of solid phase momentum and energy as opposed to o.d.e.s for primitive variables. Upon integration, the above system yields positive values of $\tilde{\rho}_s$ and T_s, and negative values of w_s and $\tilde{\rho}_g\, w_g\, z$. After each integration step, the algebraic conditions (22) can be employed for the evaluation of the gaseous phase variables.

For the problem under consideration, initial conditions are the post-shock values of the flow variables. Let the subscript '*in*' denote the initial post-shock state, and the subscript '0' denote the condition of the mixture in the quiescent pre-shock state. The solid phase equations do not admit discontinuous solutions except for contact surfaces. Therefore,

$$(\tilde{\rho}_s, w_s, T_s, d_p)_{in} = (\tilde{\rho}_s, w_s, T_s, d_p)_0, \tag{23}$$

where $(w_s)_0 = -D$. For the evaluation of the initial values of the gas flow variables, we can employ the standard gasdynamic jump relations, i.e.

$$(\tilde{\rho}_g w_g)_{in} = (\tilde{\rho}_g w_g)_0, \tag{24a}$$

$$\left(\tilde{\rho}_g w_g^2 + \tilde{\rho}_g T_g\right)_{in} = \left(\tilde{\rho}_g w_g^2 + \tilde{\rho}_g T_g\right)_0, \tag{24b}$$

$$\left(c_p T_g + 0.5 w_g^2\right)_{in} = \left(c_p T_g + 0.5 w_g^2\right)_0, \tag{24c}$$

$$z_{in} = z_0 = 1. \tag{24d}$$

The end-state conditions are those of completion of the reaction processes:

$$\text{at} \quad \xi \to -\infty : \quad z = 0, \quad \tilde{\rho}_s = 0. \tag{25}$$

For a detailed analysis of the end-state, see Powers *et al.* (1990*b*). We observe that at neither $\xi = 0$ nor $\xi = -\infty$ is there a complete set of boundary conditions. At the origin, the value of $(w_s)_0$ is unknown (because D is unknown), and at infinity, there are no explicit relations for the velocities and the temperatures. Therefore, probably the easiest way to solve this problem numerically is to select a value for the wave speed D, numerically integrate the system from 0 up to a large negative value of ξ, and then check if the end-state conditions (25) are satisfied. If they are, then the computed profiles for the flow variables, together with the value of D, constitute an admissible steady-wave solution. If this strategy is followed, then combining (23) with the following definitions,

$$C_4 = C_1 - \tilde{\rho}_s w_s, \tag{26a}$$

$$C_5 = C_2 - \tilde{\rho}_s w_s^2, \tag{26b}$$

$$C_6 = \frac{C_3 - \left(c_s T_s + 0.5 w_s^2 + q_2\right) \tilde{\rho}_s w_s}{C_4} - q_1 z, \tag{26c}$$

leads to a second-order equation for w_s,

$$\frac{2c_p - 1}{2c_p} w_s^2 - \frac{C_5}{C_4} w_s + \frac{C_6}{c_p} = 0. \tag{27}$$

Once the gas velocity has been calculated by solving the above equation, the thermodynamic variables of the gas can be computed directly by solving the algebraic equations (22). Equation (27) can also be employed for the derivation of parametric conditions for admissible steady-wave solutions. This is beyond the scope of the present study since the main motivation for steady-wave analysis is algorithm validation and checks of the accuracy of numerical results. Nonetheless, it has been numerically verified that for a wide range of physical parameters and initial conditions, the above equation possesses two real-valued solutions of which only one is physically admissible.

A steady-wave solution belonging to the class of single-front detonations has been obtained with the parameters and initial conditions that correspond to case A of § 5 below. Profiles of the flow variables for this case are plotted in figure 1. It can be verified that, owing to the high post-shock temperature, both gaseous and solid reactants begin to burn behind the leading front. The burning rate of particles is noticeably high and, as a result, the detonation is supported by the heat release from both reactions. The gaseous reaction rate, though, is much higher than that of the particle burning. Consequently, the gaseous reaction reaches completion much earlier than the completion of the processes of particle burning and temperature and velocity relaxation.

Steady-wave solutions of the second mode, the pseudo-gas detonation, could not be predicted. However, unsteady pseudo-gas detonations have been observed in some of our numerical simulations. The structure of these flows is similar to the structure of detonations in mixtures with inert particles. The leading front is supported by the heat of the gaseous reaction only. Behind the front, a long compaction zone is formed, inside which the particles burn very slowly. The propagation velocity of the tail of this zone is lower than that of the leading front. Therefore, the length of the

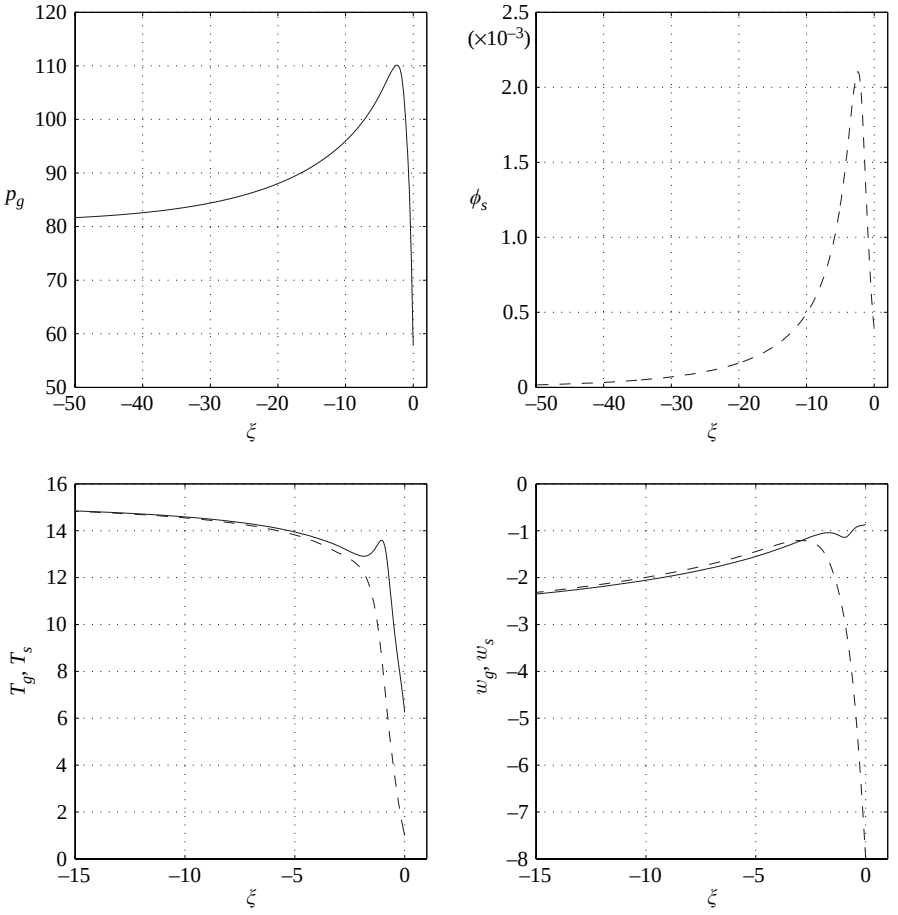

FIGURE 1. Profiles of flow quantities for a steady single-front detonation. Continuous lines correspond to gas variables, and dashed lines correspond to solid-phase variables.

compaction zone increases with time, thus prohibiting the establishment of a flow field in the form of a single travelling wave.

For the same reason (different propagation velocities of the leading front and the tail of the compaction zone), it was impossible to identify parameter values for detonations in mixtures with inert particles that resulted in flow fields consisting of a single steady wave. Nonetheless, parameter values that resulted in the formation of two steady wavefronts have been numerically identified. These fronts are the leading detonation wave and the tail of the compaction zone. In other words, the detonation wave and the tail of the compaction zone have constant but unequal velocities. This implies that the length of the compaction zone increases at a constant rate. An example of such case is Case A for inert particles described in § 5.3.

Finally, steady-wave solutions of the third mode, the pseudo-gas detonation, cannot be calculated without additional information of the strength and location of the secondary shock. Currently, it is not well understood which conditions or which particles can actually lead to the development of such a structure. For example, the simulations of Uphoff *et al.* (1995) for mixtures with aluminium particles indicate that

a steady double-front structure is indeed possible. On the other hand, the simulations of Veyssiere *et al.* (1999) suggest that such a structure is not possible for mixtures containing starch particles. Our simulations showed that secondary discontinuities can indeed develop owing to the delay in the heat release from the two reactions, but they propagate at speeds substantially different from those of the leading front. As a result, they eventually decay or overtake the leading front.

4. Description of the numerical method

The algorithm employed in this study for the solution of the governing system (7)–(8) is based on the methodology proposed by Papalexandris *et al.* (2002) for multidimensional systems of hyperbolic conservation laws with source terms. It is a high-order unsplit shock-capturing algorithm. Its design follows the spirit of the original MUSCL scheme of van Leer (1979). All terms of the governing equations are integrated simultaneously (in a single time step), thus avoiding dimensional or time splitting.

The algorithm performs the following four basic steps to advance the solution from $t = n\Delta t$ to $t = (n+1)\Delta t$.

(i) Primitive flow variables are assumed to vary linearly inside each computational cell. Their spatial derivatives are computed using a slope limiter. In the present implementation of the scheme, van Albada's limiter has been employed (van Leer 1979).

(ii) Predictions for the flow variables on the cell interfaces at $t = (n+1/2)\Delta t$ are obtained by tracing appropriate curves in the three-dimensional Euclidean space–time.

(iii) In order to take care of discontinuities, the predicted values from step (ii) are used as initial conditions for the Riemann problem of the system (7)–(8). The solution to this Riemann problem yields the final estimates for the flow variables on the cell interfaces at $t = (n+1/2)\Delta t$.

(iv) The fluxes at the interfaces are computed from the solution of the Riemann problem and the conservation laws are integrated via a finite-volume scheme.

To fix ideas, consider a hyperbolic conservation law with a source term written in integral form,

$$\frac{\mathrm{d}}{\mathrm{d}t}\int_V \sigma \,\mathrm{d}V + \int_S \boldsymbol{w}(\sigma)\cdot \mathrm{d}\boldsymbol{S} = \int_V \psi \,\mathrm{d}V. \tag{28}$$

In (28), σ is the unknown variable, $\boldsymbol{w}$ is the flux and ψ is the source term. The finite-volume scheme applied to the (i, j)th cell of an unstructured grid, reads

$$\begin{aligned}(\sigma_{i,j})^{n+1} = (\sigma_{i,j})^{n} + \frac{\Delta t\,\Delta S_{ij}}{\Delta L_{ij}}\left[(l\psi)^{n+1/2}_{i+1/2,j} + (l\psi)^{n+1/2}_{i-1/2,j} + (l\psi)^{n+1/2}_{i,j+1/2} + (l\psi)^{n+1/2}_{i,j-1/2}\right] \\ - \Delta t\left[(l\,\boldsymbol{n}_{\mathrm{c}}\cdot\boldsymbol{w})^{n+1/2}_{i+1/2,j} - (l\,\boldsymbol{n}_{\mathrm{c}}\cdot\boldsymbol{w})^{n+1/2}_{i-1/2,j} + (l\,\boldsymbol{n}_{\mathrm{c}}\cdot\boldsymbol{w})^{n+1/2}_{i,j+1/2} - (l\,\boldsymbol{n}_{\mathrm{c}}\cdot\boldsymbol{w})^{n+1/2}_{i,j-1/2}\right],\end{aligned} \tag{29}$$

where l is the length of the particular interface, ΔS_{ij} and ΔL_{ij} are the area and perimeter, respectively, of the (i, j)th cell, and $\boldsymbol{n}_{\mathrm{c}}$ is the unit vector normal to the interface. The values of the fluxes and the source term are computed via the procedure outlined in steps (ii) and (iii). These steps are described in some detail below.

Step (ii) is reminiscent of the characteristic ray-tracing for the one-dimensional gasdynamic Euler equations. According to the classical characteristic theory for hyperbolic conservation laws, the corresponding homogeneous one-dimensional

system can be decomposed into a set of o.d.e.s, $\mathrm{d}f_i/\mathrm{d}t = 0, i = 1, \ldots, 8$, so that each o.d.e. holds along the corresponding characteristic path. In other words, the decomposition reads

$$\frac{\mathrm{d}f_i}{\mathrm{d}t} = 0 \quad \text{along} \quad \frac{\mathrm{d}x}{\mathrm{d}t} = \lambda_i \quad (i = 1, \ldots, 8), \tag{30}$$

where λ_i are the eigenvalues of the one-dimensional analogue of (7)–(8), and they are given by

$$\lambda_1 = u_g, \qquad \lambda_{2,3} = u_g \pm \sqrt{\gamma p_g/\rho_g}, \qquad \lambda_4 = \lambda_1, \qquad \lambda_{6-8} = u_s. \tag{31}$$

Next, ten new quantities, $\hat{\boldsymbol{u}}_i$, having dimensions of velocity are introduced such that the system (7)–(8) can be decomposed into a set of o.d.e.s, $\mathrm{d}f_i/\mathrm{d}t = 0, i = 1, \ldots, 10$. This set consists of the eight o.d.e.s in (30), plus two additional o.d.e.s for the tangential velocity components.

Each of the ten o.d.e.s holds along the path $\mathrm{d}x_i/\mathrm{d}t = \boldsymbol{\lambda}_i + \hat{\boldsymbol{u}}_i$, where $\boldsymbol{\lambda}_i$ are the two-dimensional extensions of λ_i, i.e.

$$\boldsymbol{\lambda}_1 = \boldsymbol{u}_g, \qquad \boldsymbol{\lambda}_{2,3} = \boldsymbol{u}_g \pm \sqrt{\gamma p_g/\rho_g}\,\boldsymbol{n}, \qquad \boldsymbol{\lambda}_{4,5} = \boldsymbol{\lambda}_1, \qquad \boldsymbol{\lambda}_{6-10} = \boldsymbol{u}_s, \tag{32}$$

with $\boldsymbol{n}$ being an arbitrary but fixed spatial unit vector.

In other words, ten new convective velocities, $\hat{\boldsymbol{u}}_i$, are defined so that the system (7)–(8) can be decomposed into

$$\frac{\mathrm{d}f_i}{\mathrm{d}t} = 0 \quad \text{along} \quad \frac{\mathrm{d}\boldsymbol{x}}{\mathrm{d}t} = \boldsymbol{\lambda}_i + \hat{\boldsymbol{u}}_i \quad (i = 1, \ldots, 10). \tag{33}$$

The ten o.d.e.s are

$$\frac{\mathrm{d}f_1}{\mathrm{d}t} = \frac{\mathrm{d}\tilde{p}_g}{\mathrm{d}t} - \frac{\gamma\tilde{p}_g}{\tilde{\rho}_g}\frac{\mathrm{d}\tilde{\rho}_g}{\mathrm{d}t} = 0, \tag{34a}$$

$$\frac{\mathrm{d}f_2}{\mathrm{d}t} = \frac{\mathrm{d}\tilde{p}_g}{\mathrm{d}t} + \sqrt{\gamma\tilde{\rho}_g\tilde{p}_g}\,\boldsymbol{n}\cdot\frac{\mathrm{d}\boldsymbol{u}_g}{\mathrm{d}t} = 0, \tag{34b}$$

$$\frac{\mathrm{d}f_3}{\mathrm{d}t} = \frac{\mathrm{d}\tilde{p}_g}{\mathrm{d}t} - \sqrt{\gamma\tilde{\rho}_g\tilde{p}_g}\,\boldsymbol{n}\cdot\frac{\mathrm{d}\boldsymbol{u}_g}{\mathrm{d}t} = 0, \tag{34c}$$

$$\frac{\mathrm{d}f_4}{\mathrm{d}t} = \frac{\mathrm{d}(\boldsymbol{u}_g\cdot\boldsymbol{n}^{\perp})}{\mathrm{d}t} = 0, \tag{34d}$$

$$\frac{\mathrm{d}f_5}{\mathrm{d}t} = \frac{\mathrm{d}z}{\mathrm{d}t} = 0, \tag{34e}$$

$$\frac{\mathrm{d}f_i}{\mathrm{d}t} = \frac{\mathrm{d}\omega_i}{\mathrm{d}t} = 0 \qquad (i = 6, \ldots, 10), \tag{34f}$$

where $\omega \in \{\phi_s, u_s, v_s, T_s, N_s\}$. In (34c), $\boldsymbol{n}^{\perp}$ is the unit vector normal to $\boldsymbol{n}$.

Each of these o.d.e.s defines a manifold in the Euclidean space–time. A different choice of $\hat{\boldsymbol{u}}_i$ corresponds to a different path along the manifold defined by the ith o.d.e. Therefore, for each o.d.e. given in (34), there is an one-parameter family of convective velocities $\hat{\boldsymbol{u}}_i (i = 1, \ldots, 10)$ that allows the decomposition (33) to be valid. Carrying on with the analysis, we find that each of these convective velocities has to satisfy an inner-product relationship in order for (34) to be valid. Therefore, these

inner-product relationships (which are not presented here for the sake of brevity) can be viewed as both compatibility conditions for the proposed decomposition, and as defining relations for $\hat{\boldsymbol{u}}_i (i = 1, \ldots, 10)$. For more details, see Papalexandris *et al.* (2002).

For computational purposes, one curve from each of the 10 manifolds must be selected. In the present implementation of the algorithm, the selected curves are those for which the norms of the convective velocities $|\hat{\boldsymbol{u}}_i| (i = 1, \ldots, 10)$, attain a minimum. The list of selected convective velocities is given in the Appendix. Other choices, however, are also possible. Once the curves along the manifolds have been selected, each o.d.e. is integrated numerically up to $t = (n + 1/2)\Delta t$ along its corresponding curve. For numerical purposes, these curves are approximated by straight-line segments.

The third step of the algorithm consists of solving the one-dimensional Riemann problem for the system (7)–(8) with initial data provided by the solution of the o.d.e.s (34) along their corresponding manifolds. Since coupling between the two phases comes from the source terms only, cf. (7)–(8), it is possible to solve two separate single-phase Riemann problems: one for the gaseous phase and the other one for the solid phase. Probably the most robust implementation is to solve the two single-phase Riemann problems in the direction normal to the cell interface. Nonetheless, other possible directions are also allowed by the algorithm.

For the gaseous phase, the algorithm computes the solution to the classical gasdynamic Riemann problem with the modification that p_g and ρ_g have been substituted by $\tilde{p}_g$ and $\tilde{\rho}_g$, respectively. In other words, in the Riemann solver for the gaseous phase, the pressure and density have been replaced by the partial pressure and density. It should be pointed out that in the presence of source terms, the Riemann problem is not self-similar like the classical gasdynamic Riemann problem. Nonlinear waves are not straight lines on the (x, t)-plane because they do not move at constant speeds anymore. Yet, the solution of the Riemann problem for reacting flows converges to the solution of the classical Riemann problem as $x, t \to 0$. Therefore, for computational purposes, we can safely use the solution of the classical Riemann problem.

As far as the solid phase is concerned, we observe that equations (8) form a degenerate system of hyperbolic conservation laws. In fact, the system possesses only one distinct eigenvalue (with triple multiplicity), $\lambda = u_s$. Additionally, the gradient of the eigenvalue in phase-space is normal to the eigenvector. This implies that only contact discontinuities are permissible for the solid phase; shock waves cannot be formed. The contact discontinuities move with the characteristic speed, which is the solid-phase velocity.

Therefore, the Riemann problem for the solid phase is trivial. This means that for computational purposes the use of a solid-phase Riemann solver can be avoided. Indeed, numerical experiments showed that computing the fluxes at the interfaces using the solution of the o.d.e.s, (34), without any Riemann-solver correction is an accurate and robust procedure. A Riemann solver for incompressible solid phase equations similar to (8) has been proposed by Saurel, Daniel & Loraud (1994). More specifically, they considered six possible initial conditions, depending on the direction and magnitude of the velocity vector of the solid particles on each side of the discontinuity. For each initial condition, they presented a simple solution for the evolution of the discontinuity. When we attempted to incorporate this Riemann solver into the present scheme, we did not observe any improvement on the results. Therefore, this idea was not pursued further.

It is worth mentioning that the proposed decomposition (33) for the system (7)–(8) that was outlined above is mathematically exact and quite general. Therefore, it can be applied to an arbitrary system of multidimensional hyperbolic conservation laws. Examples include two-phase flow models that take into account particle compressibility and particle–particle interactions. Extension of the algorithm to flows with compressible particles would require an equation of state and a Riemann solver for the solid phase.

Code validation has been performed with various tests. As a first test, the code was used to simulate one-dimensional and two-dimensional purely gaseous detonations. The results obtained from these simulations were exactly the same as those reported in Papalexandris *et al.* (1997, 2002). As a second test, we performed simulations of the dusty shock-tube problem (Miura & Glass 1982). This is an inert two-phase-flow problem; the driver section of a shock tube initially contains pure gas, while the driven section contains a cloud of particles. A shock wave is formed after the burst of the diaphragm which propagates into the driven section. Our results were sufficiently close to those of Miura & Glass (1982). More specifically, the difference in the predicted shock speeds was 2.5 %, while the difference in the velocities of the contact discontinuities was approximately 4 %. Such differences are deemed small if we take into account that in the flow model of Miura & Glass (1982), the volume occupied by the particles was neglected and that the expressions for the momentum and energy exchanges between the two phases were slightly different.

As a third test, we computed some cases with reactive solid particles for which steady-wave solutions exist. The agreement between the steady-wave profiles and the numerically computed solutions was very satisfactory. Finally, a series of convergence studies was conducted to test the accuracy of the algorithm. Some results of these studies are presented below.

5. Numerical results for one-dimensional detonations

In this section, we present results from simulations of one-dimensional detonations in mixtures of gases and particles. The section is organized as follows. First, the physical parameters are selected and a length-scale analysis is presented. This analysis facilitates the estimation of the required spatial resolution for the problems of interest. Next, results for three representative cases for mixtures with reactive particles are presented. These cases correspond to different choices for the values of particle volume fraction and particle diameter in the quiescent medium, denoted by ϕ_{s0} and d_p, respectively. We have avoided cases with ϕ_{s0} so small that the continuum assumption for the solid phase could become questionable. Further, results for the same three cases but for mixtures with inert particles are presented. A discussion on the structural characteristics of the predicted flow fields and the mechanisms that created them accompanies the presentation of the numerical results. Finally, we present the results of parametric studies that we conducted in order to explore the role of certain physical parameters on the propagation and stability of two-phase detonations.

5.1. *Parameter selection and length-scale analysis*

The steady-state Zeldovich–von Neumann–Doering (ZND) profile of a purely gaseous detonation is used as the initial condition. Linear stability analysis (Erpenbeck 1964; Lee & Stewart 1990), has shown that ZND waves are stable at high overdrives, but become increasingly unstable as the overdrive decreases. In fact, numerical results

for ZND detonations at low overdrives (near unity) show that the governing system possesses the typical characteristics of chaotic systems with a small number of degrees of freedom (Papalexandris *et al.* 1997).

The numerical simulations are set up as follows. The ZND wave is placed near the left boundary and is allowed to propagate downstream, toward the quiescent two-phase mixture. The quiescent mixture is assume to be uniform, i.e. the distribution of the particle volume fraction is assumed constant. Inflow conditions (constant flow variables) have been imposed on the left boundary, while outflow conditions (zero normal gradients of the flow variables) have been imposed on the right boundary.

The half-reaction length of the ZND wave, $L_{1/2}$ is defined as the characteristic length scale. This choice is made for two reasons. First, $L_{1/2}$ is commonly used as the unit length in studies of gaseous detonations. Secondly, for the physical parameters of interest, $L_{1/2}$ is the smallest length scale of the problem (typically, $L_{1/2}$ is at the order of 1 cm). The characteristic length scale divided by the sound speed ahead of the shock provides the characteristic time scale, $t_{1/2}$.

Pressure, density and temperature are non-dimensionalized by the values of the gaseous pressure, p_0, density, ρ_0, and temperature, T_0, ahead of the shock. It should also be clarified that, throughout the paper, Mach number calculations were based on the frozen sound speed of the gas ($\sqrt{\gamma p_0/\rho_0}$), and were performed with respect to the laboratory frame of reference and not with respect to a shock-attached frame.

In the present study, the specific heat ratio is $\gamma = 1.2$, and the reaction parameters have been set to

$$K_1 = 230.75, \qquad q_1 = 50, \qquad E_a = 50. \tag{35}$$

Further, the specific heat and density of the solid phase are set at

$$c_s = 4, \qquad \rho_s = 2500. \tag{36}$$

The reaction parameters correspond to a ZND wave of overdrive factor $f = 1.6$. The overdrive factor is defined as $f = D^2/D_{CJ}^2$, where D is the velocity of the detonation wave and D_{CJ} is the velocity of the equivalent Chapman–Jouguet detonation. According to linear stability analysis (Lee & Stewart 1990), this detonation has one unstable mode, i.e. the shock pressure oscillates periodically in time. The evolution of this detonation has been studied numerically by many authors in the past (see, for example, Bourlioux, Majda & Roytburd 1991; Papalexandris *et al.* 1997; Hwang *et al.* 2000, and references therein), so that it can be considered a well-documented case. Therefore, it can serve as a reference case in order to compare the structure and propagation characteristics of two-phase detonations with those of purely gaseous ones.

Next we show that, for the above choice of reaction parameters, $L_{1/2}$ is the smallest characteristic length of the flow. In the problem under consideration, there are three additional characteristic lengths besides $L_{1/2}$. The second characteristic length is the momentum relaxation length L_u, i.e. the distance between the leading front and the point where velocity equilibrium is attained. It is given by $L_u = u_{ref}\, t_u$, where t_u is the momentum relaxation time and u_{ref} is a reference velocity that corresponds to a time-averaged difference of u_g and u_s. It is directly deduced from (10) that

$$t_u = \frac{\rho_s\, d_p^2}{18\,\mu\, c_D}, \tag{37}$$

where $c_D > 1$, cf. (16), and $\mu > 1.71 \times 10^{-5}$, cf. (13). The smallest particle diameter that has been considered in the present study is $d_p = 0.0005\, L_{1/2}$. This implies that

$$t_u \geqslant 2\, t_{1/2}. \tag{38}$$

In turn, this suggests that even if we assume u_{ref} to be as low as the speed of sound ahead of the precursor shock, $\sqrt{\gamma p_0/\rho_0}$, the following inequality is valid,

$$L_u \; > \; 2L_{1/2}. \tag{39}$$

The third characteristic length of the problem is the length required for thermal equilibrium, L_T. It is given by $L_T = u_{ref}\, t_T$, where t_T is the thermal relaxation time. From (11), it is deduced that

$$t_T = \frac{\rho_s\, d_p^2\, c_s\, Pr}{6\, \mu\, c_p\, Nu}. \tag{40}$$

Equation (40) combined with (37) yields

$$t_T = \frac{3\, c_s\, c_D\, Pr}{c_p\, Nu}\, t_u. \tag{41}$$

With the selected values for c_s, c_p and Pr, we conclude that

$$t_T \geqslant t_u \;\Rightarrow\; L_T \geqslant L_u. \tag{42}$$

The fourth characteristic length is the distance that a particle has travelled until it burns completely, L_b. It can be estimated by $L_b = u_s\, t_b$, where t_b is the particle life time and u_s is the average particle velocity. Substituting this average velocity in (8*a*) and (8*d*) and combining (4) yields

$$\frac{\mathrm{d}d_p^2}{\mathrm{d}t} = -\frac{K_2}{3}, \tag{43}$$

which upon integration gives

$$t_b = \frac{3d_p^2}{K_2}. \tag{44}$$

In the present study, the non-dimensionalized value of K_2 was set at $K_2 = 2 \times 10^{-7}$, whereas the smallest particle diameter considered was $d_p = 5 \times 10^{-4}$. Therefore, we conclude that, for the cases examined herein, $t_b \geqslant 3.25\, t_{1/2}$. This implies that the particles burn at least 3.25 times slower than the gas (in fact they burn much slower). In turn, this means that even if we assume particle velocities as low as the speed of sound in the quiescent medium, the following inequality is valid

$$L_b \geqslant 3.25 L_{1/2}. \tag{45}$$

From the inequalities (38), (41) and (44), we deduce that $L_{1/2}$ is the smallest characteristic length of the problem. In other words, the Arrhenius kinetics law is the stiffest term among all source terms of the governing system (7)–(8). Therefore, for grid selection purposes, we can rest assured that all length scales are well resolved if the (gaseous) reaction zone is well resolved. In the present study, the grid resolution was set at 20 points per $L_{1/2}$, unless otherwise noted.

5.2. *Mixtures with reactive particles*

The parameters for the particle burning are ,

$$T_{ign} = 4, \qquad K_2 = 2 \times 10^{-7}, \qquad q_2 = 67. \tag{46}$$

These values are very close to those used by Khaisanov & Veyssiere (1996) in their reaction model.

Case A. In this case, the initial particle volume fraction, ϕ_{s0}, and the initial particle diameter, d_{p0}, are

$$\phi_{s0} = 0.0004, \qquad d_{p0} = 0.001. \tag{47}$$

This initial condition results in the establishment of a steady wave; the numerical results show that the propagation velocities of the front and the reaction zones remain constant with time. More specifically, this is a case of a single-front detonation because it is supported by energy release from both gaseous and solid-phase reactions.

Once the leading front encounters the two-phase mixture, part of the front reflects back and propagates upstream, while the other part keeps propagating downstream through the mixture. Therefore, the precursor shock of the detonation wave has less strength than that of the ZND detonation. This implies lower shock pressure and temperature, as well as lower detonation velocities. For this particular case, the drop in detonation velocity is approximately 9%. The particle Reynolds number, equation (15), attains a maximum value immediately behind the leading shock; max $Re \simeq 700$.

Plots of various flow variables at $t = 200\, t_{1/2}$ are shown in figure 2. The plotted variables are: gas pressure p_g and temperature T_g, Mach number (for the gaseous phase) in the laboratory coordinate frame, reactant mass fraction z, and solid volume fraction ϕ_s. These plots show that the particle volume fraction increases inside the thin gaseous reaction region, right behind the leading front. When the particle temperature T_s reaches the ignition temperature T_{ign}, the particles begin to burn, thus their concentration is reduced. However, the rate of particle burning is much slower than that of the gaseous reaction. As a result, their reaction zone extends over a large region, approximately $25\, L_{1/2}$.

It is also worth mentioning that both the equivalent case of a purely gaseous detonation and the equivalent case with inert particles (which is described below) result in pulsating detonations. The instabilities observed in those detonations are the result of coupling between entropy waves and heat release governed by Arrhenius reaction kinetics. The suppression of the instability in the present example is due to the introduction of an additional reaction (particle burning) that does not follow Arrhenius kinetics. Therefore, addition of reactive particles in a combustible gas suppresses the instabilities of the detonation front, but reduces its propagation velocity (with respect to the velocity of the corresponding purely gaseous detonation).

The accuracy of the simulation is first checked via comparisons with the steady-wave profiles computed via numerical solution of the system (21)–(22). The percentage error in the computation of the flow variables is plotted in figure 3. Overall, the accuracy of the simulation is quite satisfactory; for example, the maximum computational error in T_g was 0.7 %. The error peaks right behind the leading front and then decreases rapidly. This is typical of shock-capturing schemes; the error peak behind the leading front is due to the additional artificial dissipation that is required near discontinuities for the stability of the computation.

A grid-convergence study for this case has also been performed. Numerical convergence is tested via two quantities, namely, the average wave speed, D_{av}, and a discrete version of the L_1 norm of the error in the prediction of the pressure. The

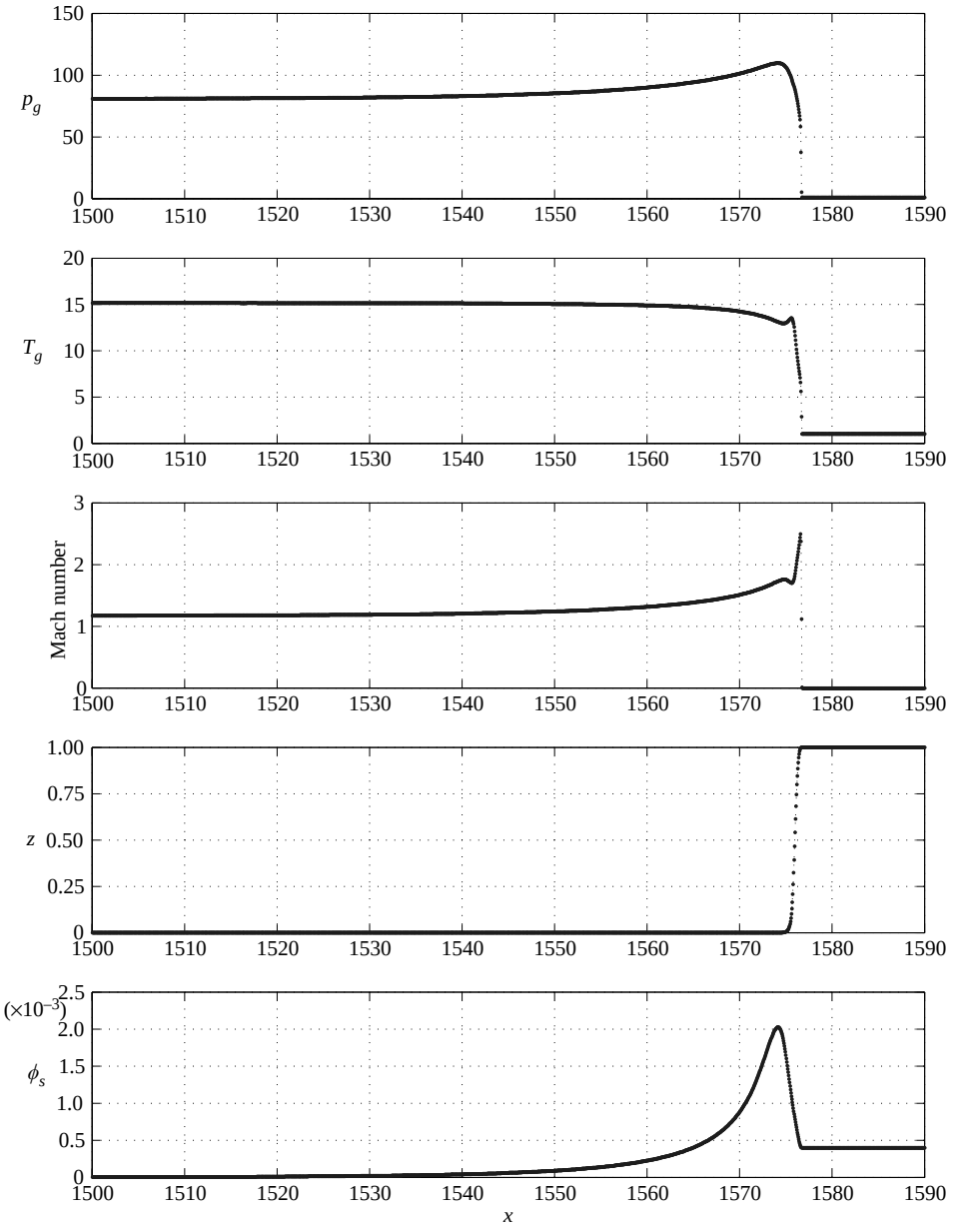

FIGURE 2. Case A, reactive particles. Spatial profiles of flow variables at $t = 200\, t_{1/2}$.

average wave speed is a global quantity of detonating flows commonly used as a measure of the accuracy of simulations. In fact, studies have shown that in under-resolved simulations, the errors in the average wave speed can be very large (see Bourlioux *et al.* 1991 and references therein). The variation of the predicted average wave speed (up to time $t = 80t_{1/2}$) with the grid resolution is shown in the first part of figure 4. It can be verified that the differences between successive approximations decay rapidly as the grid is refined.

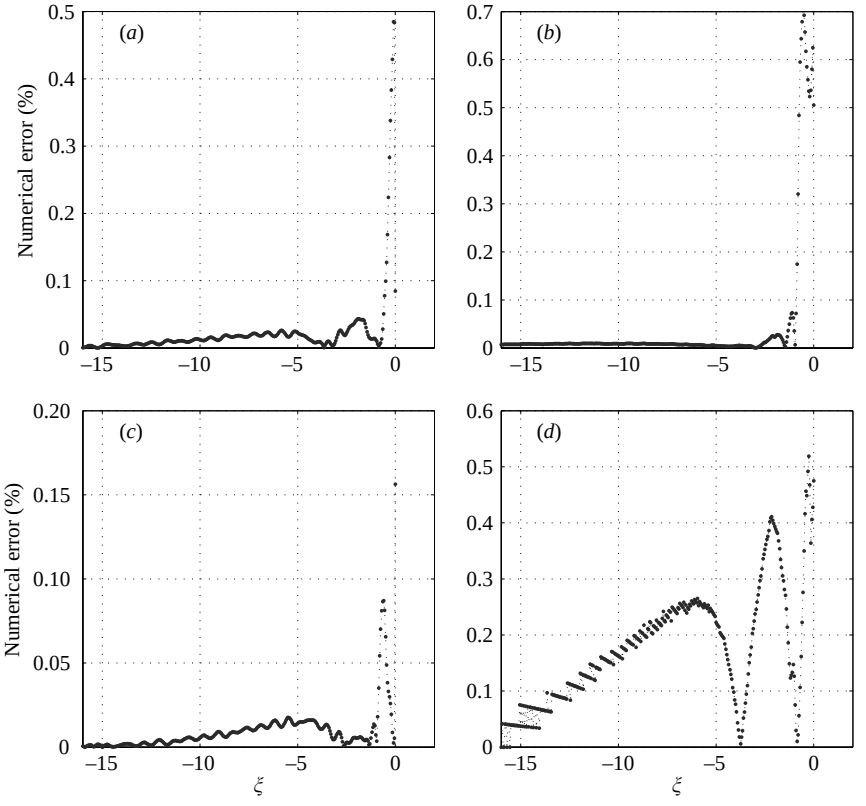

FIGURE 3. Case A, reactive particles. Percentage error of the numerical results. (*a*) Gas pressure. (*b*) Gas temperature. (*c*) Gas velocity. (*d*) Particle volume concentration.

The L_1 norm of the numerical error is also frequently used as an indicator of numerical accuracy (see Gonthier & Powers 2000). It is defined as

$$E_{\mathrm{N}}(t) = \frac{1}{N} \sum_{j=1}^{N} |p_j(t) - \hat{p}_j(t)|, \tag{48}$$

where N is the number of computational cells of the domain, and p_j and $\hat{p}_j$ are the computed and exact values of the pressure, respectively, non-dimensionalized by p_0. Values of $\hat{p}_j$ are calculated by solving the steady-wave equations (21) and (22). In the present study, instead of measuring the error over the entire computational domain, we measured it over a subdomain that covers 60 half-reaction lengths, starting just in front of the leading front. In other words, we have excluded the area of quiescent mixture ahead of the front and the area far behind the leading front where the flow quantities remain constant. Results of the numerical error at $t = 80\, t_{1/2}$ are plotted in figure 4(*a*). For resolutions of up to 20 points/$L_{1/2}$ the convergence rate is almost constant and equal to, approximately, 1.89. At higher resolutions, however, the convergence rate is decreased. This is not surprising because diffusive errors due to shock capturing do not scale with resolution. (On the contrary, numerical errors in smooth parts of the flow do scale with resolution). Therefore, the relative importance of shock-capturing errors increases as the grid is refined.

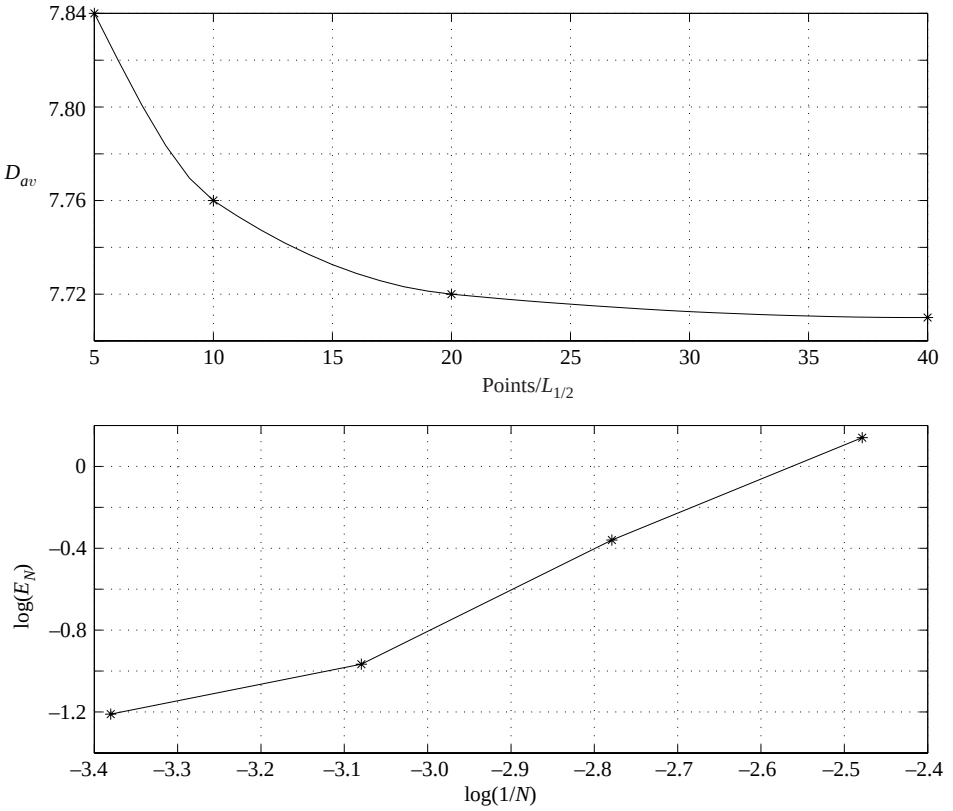

FIGURE 4. Grid convergence study for Case A with reactive particles.

Case B. In this case, the particle volume fraction of the mixture ahead of the shock is increased, whereas the initial particle diameter has been kept the same,

$$\phi_{s0} = 0.001, \qquad d_{p0} = 0.001. \tag{49}$$

As in the previous case, a steady single-front detonation wave is established. Spatial profiles of flow variables for this case are plotted in figure 5. In general, the resulting detonation structure is very similar to that observed in Case A. The only differences are in the detonation speed and the length of the particle burning zone: higher particle volume fractions result in lower speeds and longer reaction zones. Another important characteristic of this case is that the gaseous flow becomes sonic (in the inertial frame of reference) at the end of the particle burning zone. At this location, both reactions are completed and, therefore, the sound speed equals the frozen sound speed $\sqrt{\gamma p_0/\rho_0}$. As mentioned above, the establishment of a stable detonation front is due to the reactivity of the solid particles. Error analysis and grid convergence tests have also been performed for this case, yielding results similar to those for Case A.

Case C. In this case, we considered larger particle diameters,

$$\phi_{s0} = 0.001, \qquad d_{p0} = 0.005. \tag{50}$$

The Reynolds number of the particles behind the shock is, approximately, $Re \simeq 3500$. Pressure profiles at various times are shown in figure 6, and profiles of the various flow variables at $t = 200\, t_{1/2}$ are shown in figure 7. These results confirm the establishment of a single-front detonation. As in Cases A and B, the gaseous reaction takes place

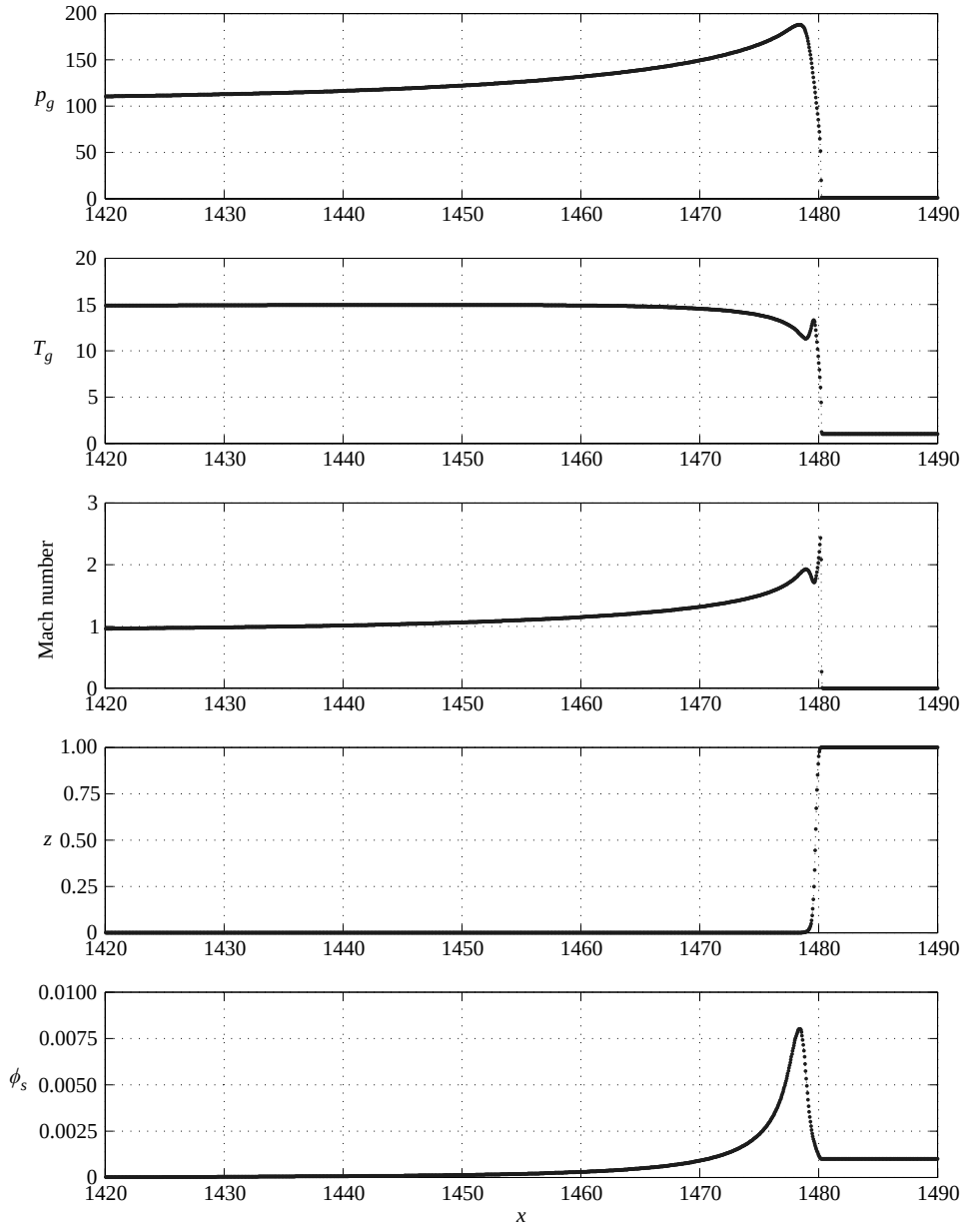

FIGURE 5. Case B, reactive particles. Spatial profiles of flow variables at $t = 200\, t_{1/2}$.

inside a thin region that is attached to the leading shock. At the same time, part of the energy that is released from the gaseous reaction is transferred to the particles. In turn, the particle temperature T_s increases rapidly and becomes higher than T_{ign}, triggering the burning of the particles. This reaction, however, does not progress as fast as the gaseous reaction and, as a result, the particle compaction zone extends over a large distance in the wake of the leading front.

A detailed study of some important physical parameters of the flow has also been performed and is described herein. We begin with the effect of the particle reactivity,

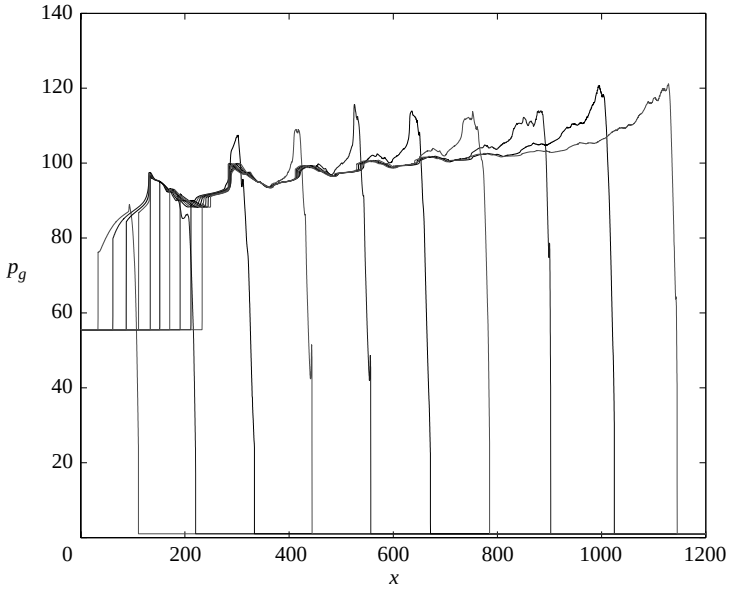

FIGURE 6. Case C, reactive particles. Spatial profiles of gas pressure at various times, $t = 20, 40, 60, \ldots, 200$.

i.e. the value of the time constant K_2 of the particle burning law. Our simulations predicted that the detonation velocity increases with the particle reactivity. Results from our parametric study on particle reactivity are plotted in figure 8 (initial conditions and constants taken from Case A). This figure contains plots of the average wave speed (up to $t = 80\, t_{1/2}$), and the maximum value of ϕ_s as functions of K_2. These plots indicate that these two quantities depend monotonically on K_2, but it also appears that they both have an asymptotic limit. This would imply that increases of the particle reactivity beyond a critical value will have no significant effect on the detonation velocity.

The role of the mixture's particle volume fraction, ϕ_{s0} is discussed next. The dependence of the average wave speed on ϕ_{s0} is monotonic and is plotted in figure 9. As the particle volume fraction ϕ_{s0} increases, the shock speed drops. Furthermore, it was predicted that sufficiently high particle volume fractions can cause detonation quenching regardless of the particle reactivity. This is explained as follows. For the particle burning to begin, the solid phase temperature T_s must reach a certain threshold. For sufficiently high particle concentrations, a substantial amount of momentum and energy transfer from the gas to the particles has already taken place by the time the solid phase temperature reaches that threshold. This causes a dramatic drop in the strength of the leading front and in the detonation velocity.

The effect of the initial particle diameter, d_{p0}, has also been examined numerically. The dependence of the average wave speed on d_{p0} for various values of ϕ_{s0} is plotted in figure 10. These plots suggest that as d_{p0} drops, the detonation velocity increases. This is explained by the fact that the rate of particle burning is inversely proportional to the second power of d_{p0}, cf. (12). Further, we note that the effect on wave speed is more pronounced at high ϕ_{s0}. For example, the rate $\Delta D_{av}/\Delta d_{p0}$ increases rapidly for $d_{p0} < 0.001$.

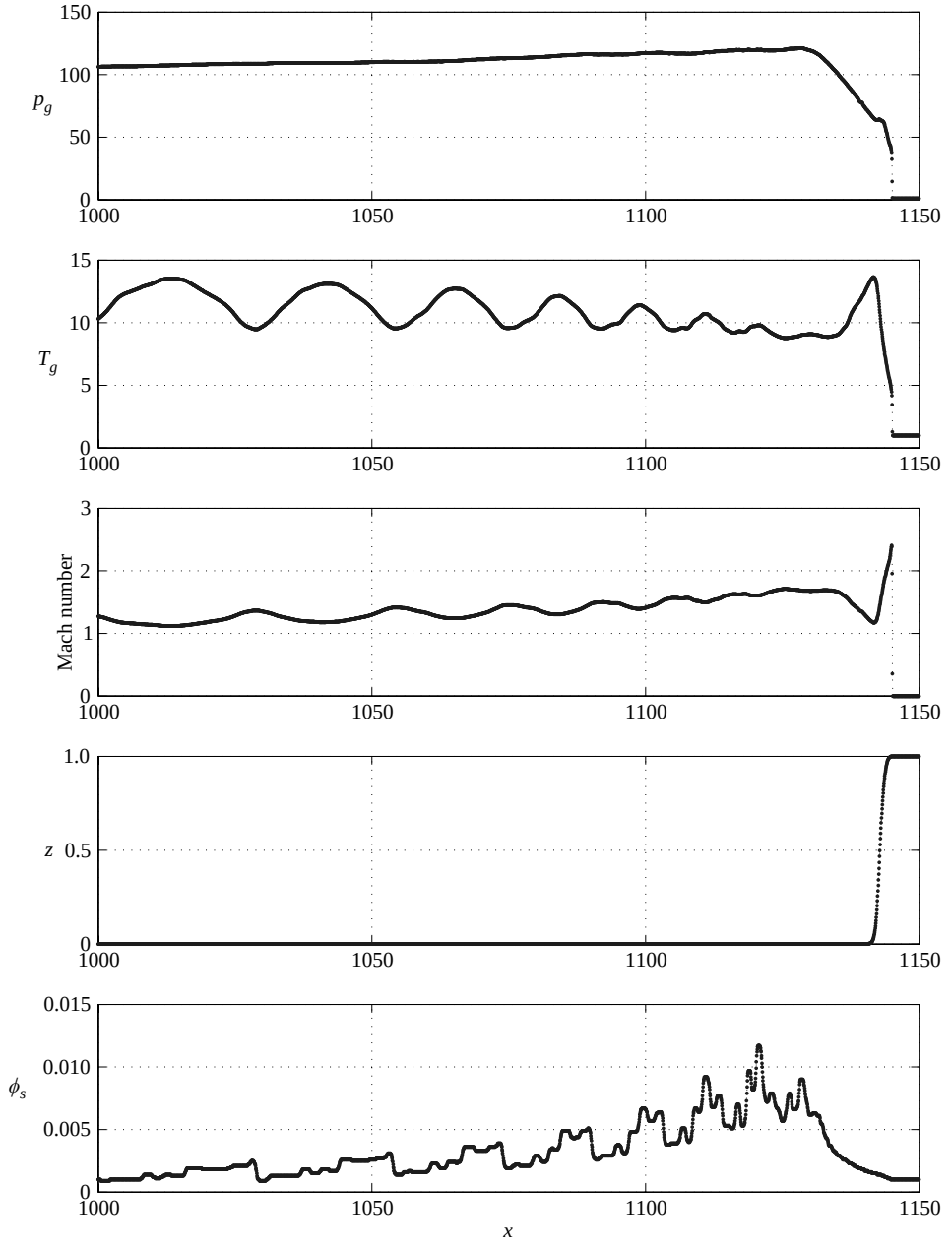

FIGURE 7. Case C, reactive particles. Spatial profiles of flow variables at $t = 200\ t_{1/2}$.

Finally, a set of numerical simulations with different overdrive factors for the initial ZND wave has also been conducted. More specifically, we considered ZND waves at overdrives of $f = 1.3$ and $f = 1.1$. It was predicted that adding reactive particles to a detonatable gas decreases always the detonation velocities. It was further predicted that the percentage of the velocity decrease is higher in the regime of low overdrives.

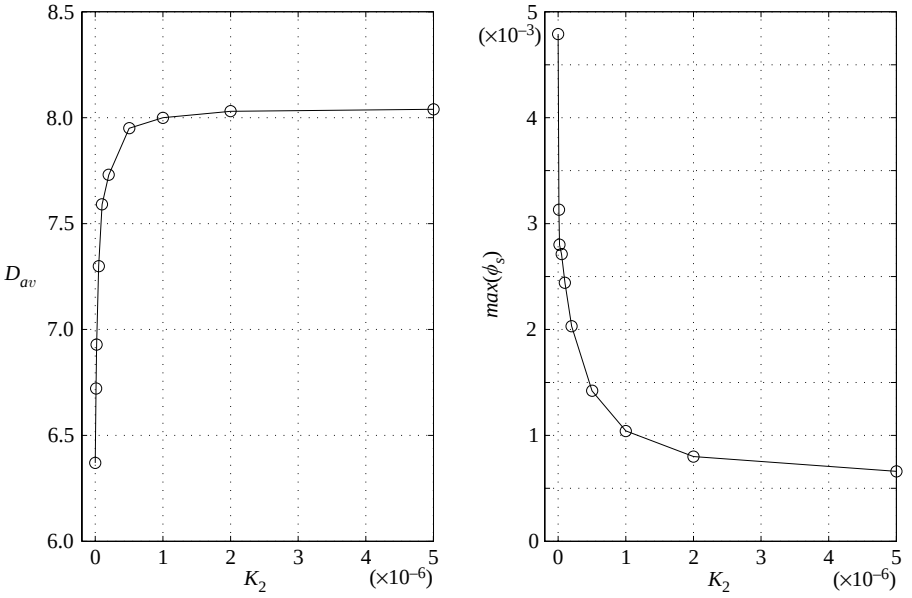

FIGURE 8. Reactive particles, Case A. Variation of the average wave speed and maximum particle volume fraction with respect to particle reactivity.

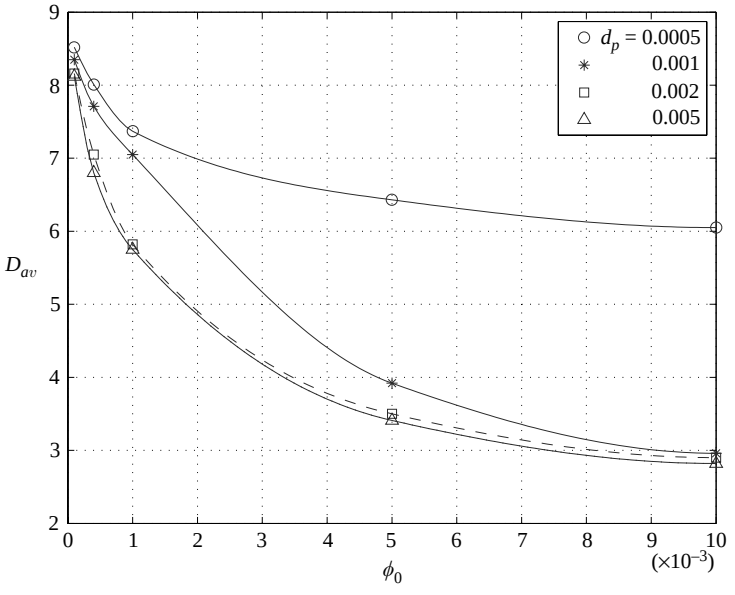

FIGURE 9. Reactive particles: variation of the average wave speed with respect to initial particle volume fraction.

5.3. *Mixtures with inert particles*

This subsection contains numerical results for two-phase detonations with inert particles. The same cases as in the previous subsection have been chosen; the only difference is that the particle burning rate is now set to zero, i.e. $K_2 = 0$, $q_2 = 0$. Owing

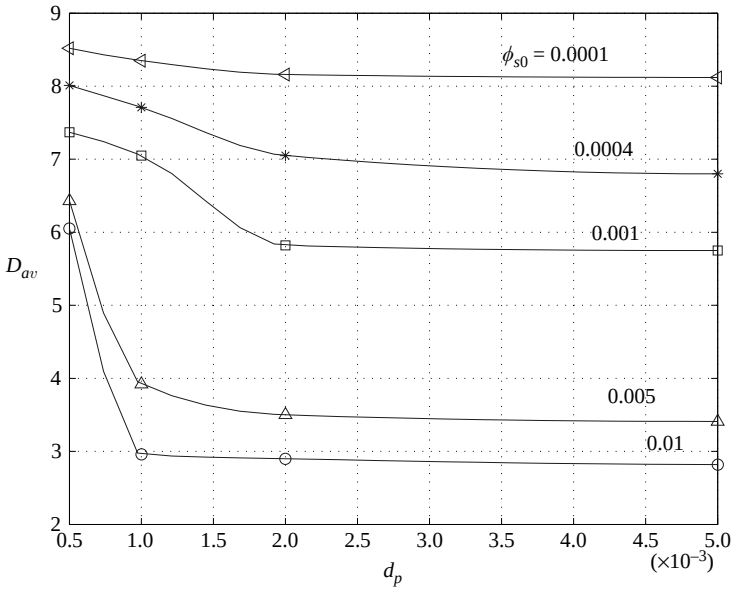

FIGURE 10. Reactive particles: variation of the average wave speed with respect to particle diameter.

to the non-reactivity and incompressibility of the particles, the particle diameter remains constant: $d_p = d_{p0}$ at all times.

Case A ($\phi_{s0} = 0.0004,\ d_{p0} = 0.001$). Profiles of the gas pressure at various times are plotted in figure 11. The plots show that the detonation wave is periodic (the shock pressure oscillates with time). In other words, this is a case of a pulsating detonation just like the equivalent purely gaseous detonation. It can also be verified that the post-shock pressure is considerably lower than in the equivalent case with reactive particles, implying lower detonation velocities. More specifically, the decrease of the detonation velocity is of the order of 25% (with respect to the case with reactive particles).

Plots of various flow variables at $t = 200\, t_{1/2}$ are shown in figure 12. These plots show that although the leading front has less strength, the shock temperature is still high enough to initiate rapid burning of the gas in a thin region immediately after the leading front. The gaseous flow remains supersonic in the entire area behind the shock. The (initially at rest) solid particles are being accelerated by the leading shock as it propagates through the mixture. In a sense, the particles are been 'pulled' by the shock, thus resulting in the formation of a compaction zone whose length increases with time. The numerical results suggest that the large values of the solid volume fraction inside the compaction zone can be related to increases of the gas density inside this region. In other words, the ratio of ϕ_s inside the compaction zone to ϕ_{s0} is very similar to the ratio of ρ_g inside this zone to ρ_0. This is consistent with solid particles that are nearly acting as tracers, i.e. they have a very fast response time and, therefore, their concentration scales with the density of the surrounding fluid.

To further explore the capabilities and limitations of the proposed algorithm, a grid-convergence study was also performed for this case.The variation of the average wave speed, D_{av} (up to time $t = 80\, t_{1/2}$), with the grid resolution is plotted in figure 13. It can be verified that the differences between successive approximations decay rapidly as the grid is refined. Examination of the profiles of the flow quantities obtained

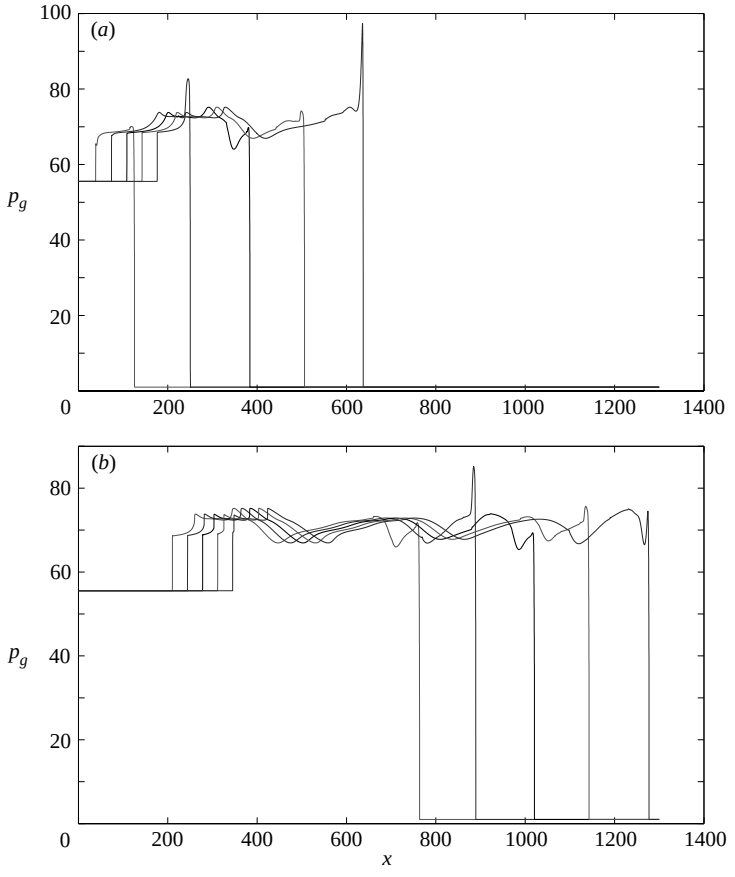

FIGURE 11. Case A, inert particles. Spatial profiles of gas pressure at various times, (*a*) $t = 20, 40, 60, 80, 100$, (*b*) $t = 120, 140, 160, 180, 200$.

with grid sizes in the range of 10–80 points/$L_{1/2}$ showed that the only observable difference is at the prediction for the spike of the particle volume fraction at the tail of the compaction zone (cf. figure 12). This difference might simply indicate that higher resolutions are required at this region of the flow. The possibility, however, that this spike is a numerical artefact cannot be excluded. For example, it might be a by-product of the smearing of the initial discontinuity on the particle volume fraction. Nonetheless, differences between predictions with successive grid refinement for the value of this spike are becoming smaller as time increases. We also note that this spike has no effect on the evolution of the detonation wave because its distance from both the leading front and the reaction zone increases with time.

Case B ($\phi_{s0} = 0.001,\ d_p = 0.001$). Profiles of the gas pressure at various times are plotted in figure 14, while profiles of the flows variables at $t = 200\, t_{1/2}$ are shown in figure 15. The increase in a ϕ_{s0} results in a further reduction of the shock strength. The shock temperature is not high enough to initiate rapid gas burning as in Case A. Instead, a long induction region, is formed behind the leading front. Inside this region, the gas burns slowly, resulting in a slow increase in temperature. When the gaseous temperature eventually becomes high enough, a thin zone of rapid burning is established.

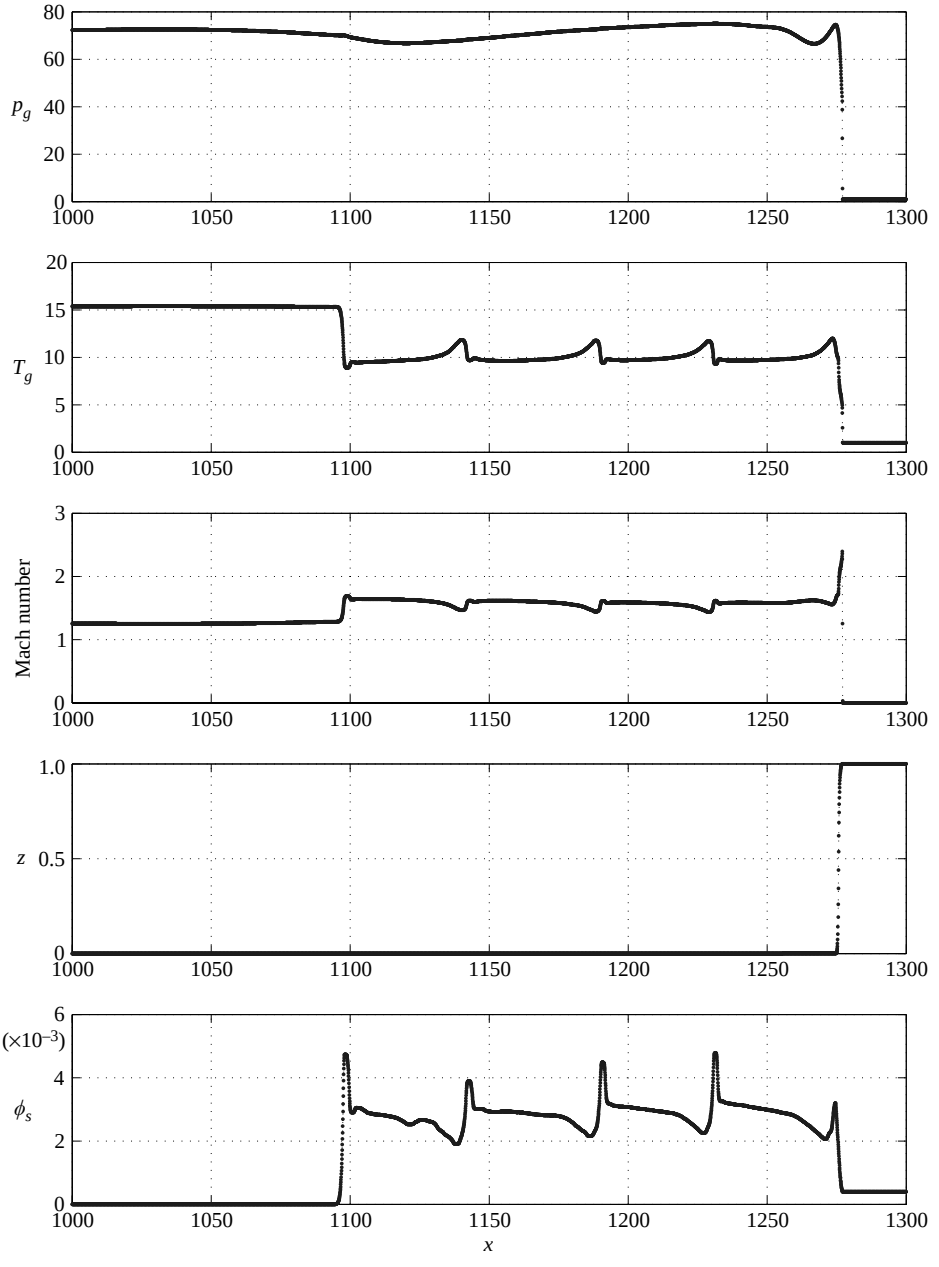

FIGURE 12. Case A, inert particles. Spatial profiles of flow variables at $t = 200\, t_{1/2}$.

Another difference from the previous case is that there is little spatial variation of the pressure field behind the shock. Further, the shock pressure does not oscillate with time, but remains constant, implying that the shock speed is also constant. The velocity of the rapid-burning zone is also constant, but lower than the shock speed. Therefore, the distance between the leading front and the rapid-reaction zone increases at a constant rate. In other words, this detonation quenches. The velocity

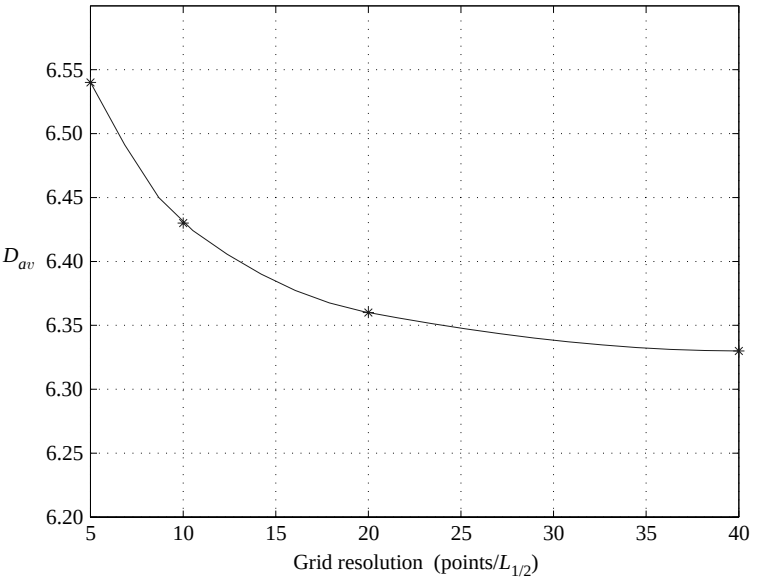

FIGURE 13. Case A, inert particles. Variation of the average wave speed D_{av}, up to $t = 80t_{1/2}$, with grid resolution.

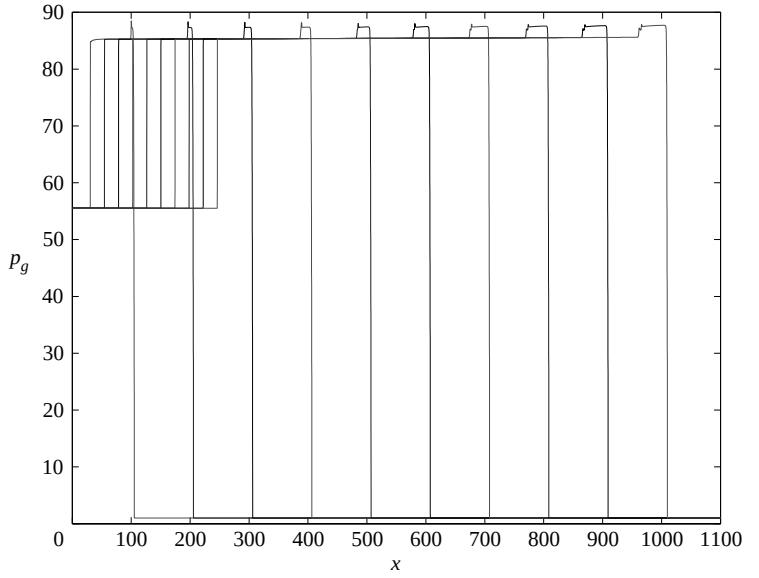

FIGURE 14. Case B, inert particles. Spatial profiles of gas pressure at various times, $t = 20, 40, 60, \ldots, 200$.

of the tail of the compaction is also constant, albeit lower than the velocity of the rapid-burning zone.

It is worth mentioning that the gaseous flow is supersonic everywhere behind the leading front. Numerical experiments showed that if the flow at the end of the reaction zone is supersonic, then this zone is always located ahead of the tail of the compaction zone, even if the detonation quenches. Further, when this condition holds, the particle

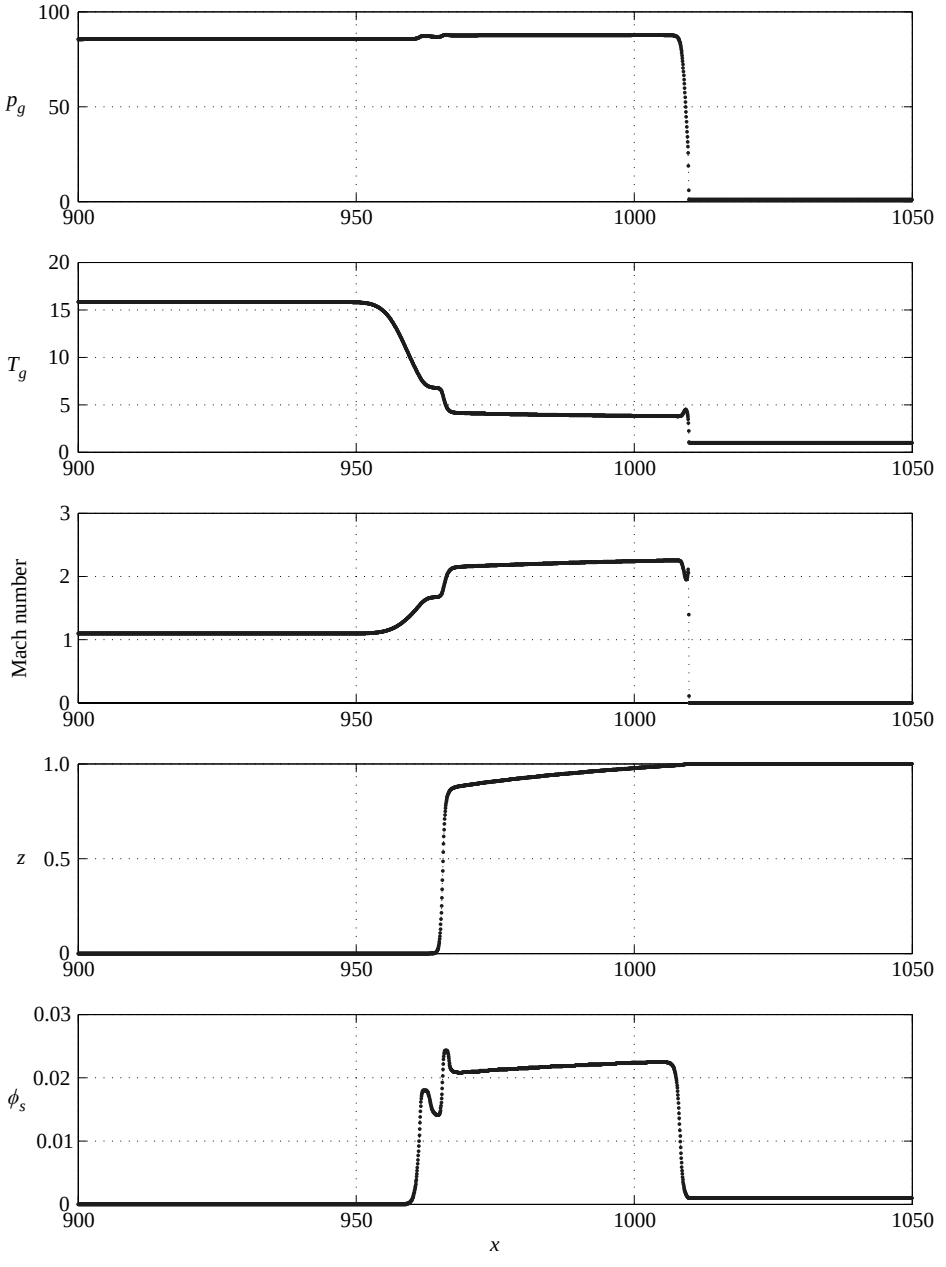

FIGURE 15. Case B, inert particles. Spatial profiles of flow variables at $t = 200\, t_{1/2}$.

volume fraction inside the compaction zone does not increase with time. On the other hand, if the flow at the end of the reaction zone is subsonic, then this zone becomes a deflagration propagating at speeds lower than those of the compaction zone. In such cases, ϕ_s monotonically increases with time.

Case C ($\phi_{s0} = 0.001,\ d_p = 0.005$). Results for the pressure at various times are plotted in figure 16, while results for various flow variables at $t = 200\, t_{1/2}$ are plotted in figure 17. These plots show that the structure of this detonation is very

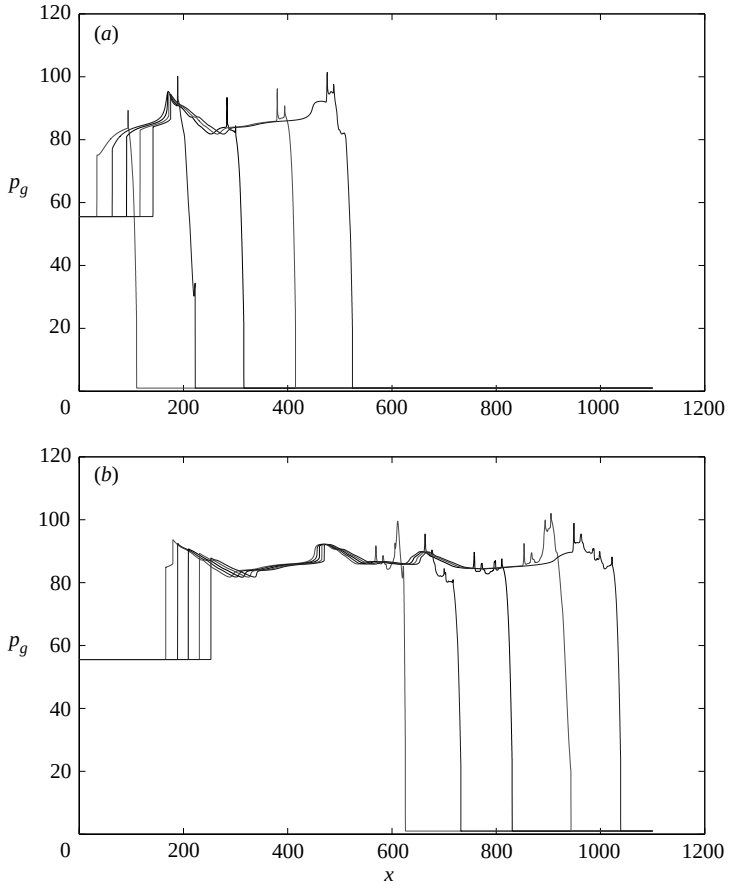

FIGURE 16. Case C, inert particles. Spatial profiles of gas pressure at various times, (*a*) $t = 20, 40, 60, 100$, (*b*) $t = 120, 140, 160, 180, 200$.

similar to those of purely gaseous detonations at low overdrive factors (Papalexandris *et al.* 1997). In particular, there is formation of pockets of unreacted material, as well as formation of secondary shock waves behind the leading front.

The temperature behind the shock, figure 17, is not high enough to sustain a rapid-burning zone. On the other hand, the increased value of the particle diameter implies smaller surface area (under constant ϕ_{s0}) of the solid phase, hence smaller momentum and energy losses for the gas. This has two consequences. First, it does not allow the formation of a long induction zone and quenching of detonation. Instead, it results in the formation of pockets of unreacted material behind the leading front. Secondly, it prohibits high particle volume fractions in the compaction zone behind the front; the values of ϕ_s remain at levels close to ϕ_{s0}.

Inside the pockets of partially unreacted gas, the reaction progresses slowly owing to relatively low temperature. Once the temperature becomes high enough, the reaction rate is increased, resulting in an explosion. Two shock waves moving in opposite directions are generated by this explosion. The shock wave that propagates downstream eventually overtakes the leading front. The strength of these secondary shock waves is quickly diminished owing to the presence of solid particles. (By contrast, the strength of these waves in purely gaseous detonations in the highly

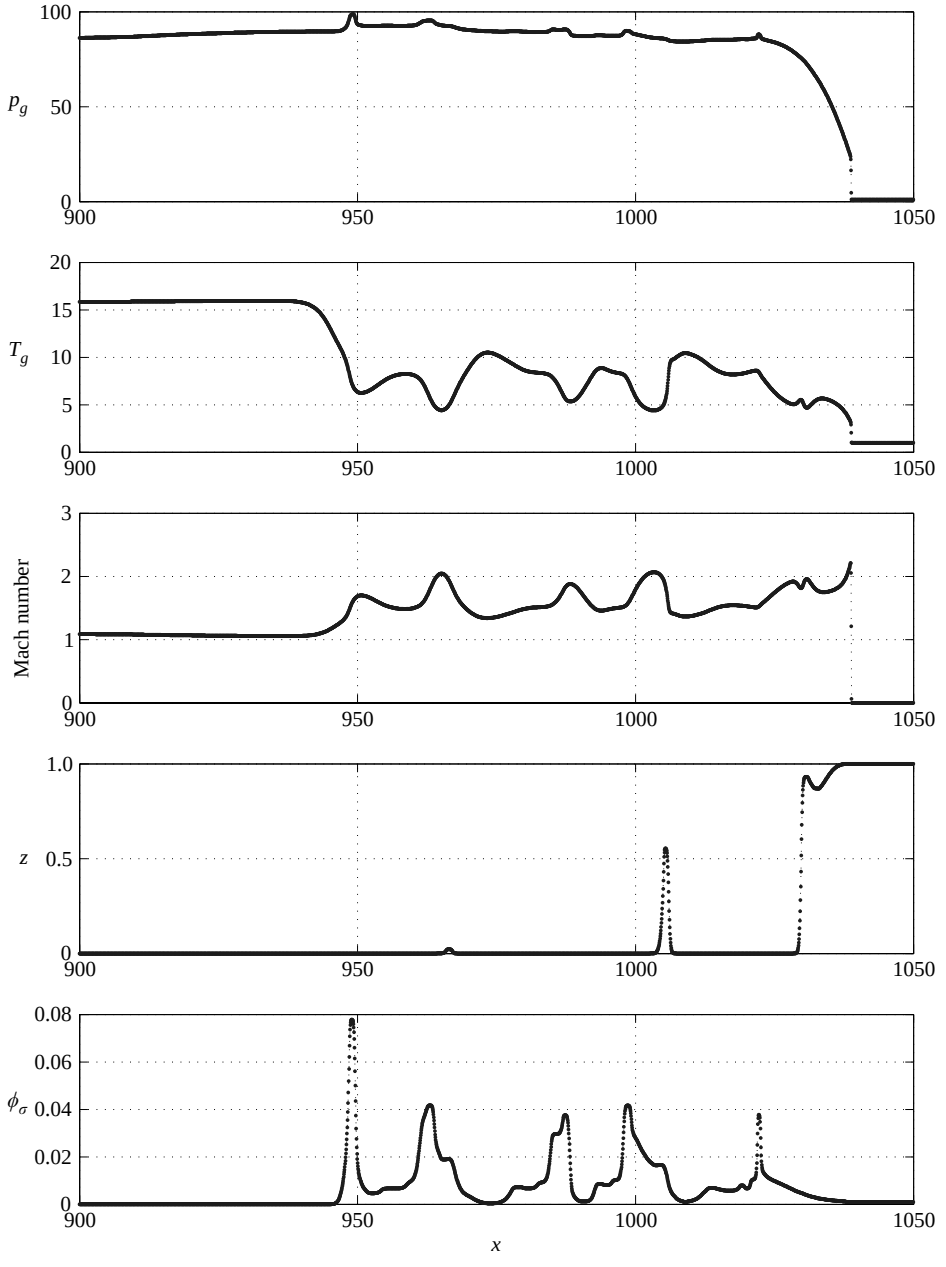

FIGURE 17. Case C, inert particles. Spatial profiles of flow variables at $t = 200\, t_{1/2}$.

unstable regime is substantial; see Papalexandris *et al.* 1997). This implies reduced shock-pressure variations owing to shock-overtakings.

Next, we discuss the effect of the particle volume fraction, particle diameter and overdrive of the initial front in two-phase detonations with inert particles. The simulations of the present study confirmed that the detonation velocity, D_{av}, varies monotonically (decreases) with particle volume fraction. Figure 18 contains plots of the variation of the average leading-shock speed, D_{av}, as a function of ϕ_{s0} at various

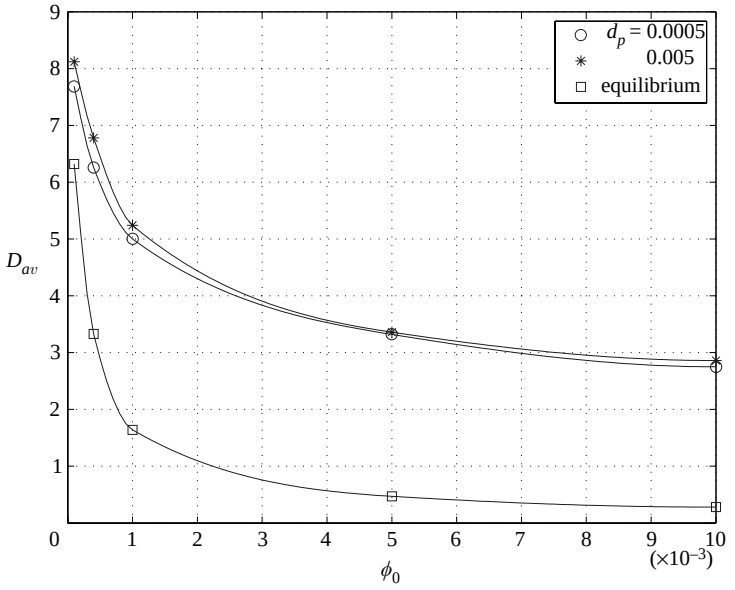

FIGURE 18. Inert particles: variation of the average wave speed with respect to initial particle volume fraction.

particle diameters. It can be observed that the drop of D_{av} in the region of small ϕ_{s0} is quite large. However, at larger particle volume fractions, the rate of decrease of D_{av} drops significantly, and it appears that D_{av} approaches an asymptotic value. This region of slow decrease of the shock-speed corresponds to quenched detonations.

In other words, increase of the particle volume fraction of the mixture leads quickly to quenching of detonations (in the cases examined herein this occurs at, approximately, $\phi_{s0} = 0.0015$). Beyond the quenching limit, the leading shock has already lost most of its strength. Further increase of ϕ_{s0} has only a minor effect on its (already weakened) strength. Figure 18 also includes a plot of the dependence of the equilibrium shock speed on ϕ_{s0}. As in the case of the direct simulations, at small ϕ_{s0} the equilibrium shock speed decreases significantly, but at higher ϕ_{s0} the decrease is much slower. Nonetheless, the predicted shock speeds for two-phase detonations are considerably higher than the equivalent equilibrium speeds, confirming the assumption that the mixture right behind the leading front is far from phase equilibrium.

The effect of particle diameter on the shock speed, for various ϕ_{s0} is plotted on figure 19. We observe that D_{av} increases monotonically with the particle diameter, independent of the value of the initial particle volume fraction. However, this increase is very small. For example, at $\phi_{s0} = 10^{-4}$, an order of magnitude increase on d_p (from 0.0005 to 0.005) produces only a 5.5% increase on D_{av}. Lafitte & Bouche (1959) explained the decrease of detonation velocities with decreasing d_p by arguing that smaller d_p under constant ϕ_{s0} results in larger surface area of particles. This implies intensified momentum and energy transfer from the gas to the particles. Our simulations indicated that d_p has a direct effect on the particle concentration in the compaction zone; smaller particle diameters result in larger particle concentrations. This phenomenon is in accordance with the above argument by Lafitte & Bouche (1959) and can be related to the mechanisms that cause deceleration of the front.

As noted earlier, however, if the particles are reactive, the effect of particle diameter is the opposite. Both our simulations that were presented above and those conducted

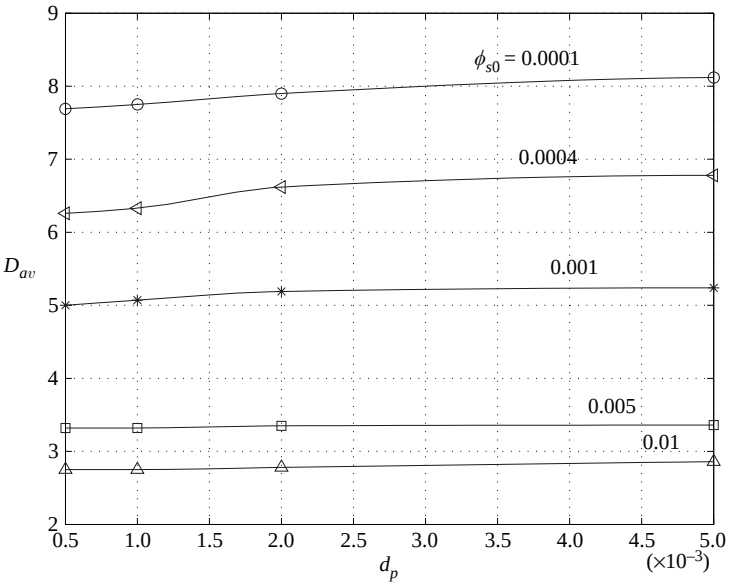

FIGURE 19. Inert particles: variation of the average wave-speed with respect to particle diameter.

by Loth *et al.* (1997) predicted that in mixtures with reactive particles, smaller diameters result in higher detonation speeds. This occurs because smaller d_p implies faster particle burning, cf. (12). Obviously, the dependence of momentum transfer between the two phases on the surface area is also present in mixtures of reactive particles. The increased momentum transfer, however, is overcompensated by the increase in the rate of heat release due to particle burning.

Numerical simulations with different overdrive factors have also been performed. It was predicted that the effect of adding inert particles in a gaseous combustible mixture is the same, regardless of the overdrive of the initial detonation. It was predicted that the effect of the particle addition is slightly more pronounced in lower overdrives. In other words, for fixed ϕ_{s0}, the percentage of the drop in the detonation velocity is slightly higher at low overdrives. Nonetheless, the basic trend that was described earlier (large velocity drops at small ϕ_{s0} and detonation quenching at a critical value of ϕ_{s0}) is always present regardless of the overdrive. Another result of our study is that even gaseous detonations that exhibit highly unstable behaviour (such as those with overdrive factors close to unity) can be stabilized with the addition of solid particles.

6. Numerical results for two-dimensional detonations

In this section, we present numerical results for two-dimensional detonations in mixtures of gases and solid particles. The same three cases as in the previous section have been considered. The main objectives of this study are to gain insight into the fundamental mechanisms that govern such flows, to investigate the effects of multidimensionality, and to make comparisons between the structures of purely gaseous and two-phase detonations.

Linear stability analysis of two-dimensional ZND waves predicts that in a wide range of reaction parameters these flows can become unstable (Yao & Stewart 1996;

Clavin, He & Williams 1997). These studies show that such flows are unstable unless the activation energy is very small. Direct numerical simulations of two-dimensional ZND waves have confirmed these results (see, for example, Oran, Kailasanath & Guirguis 1988; Bourlioux & Majda 1992; Papalexandris *et al.* 2002; and references therein). The most noticeable feature of two-dimensional purely gaseous detonations is the formation of triple points on the leading front. The triple points have a non-zero transverse velocity component and eventually collide with each other. These collisions give rise to strong explosions that produce high over-pressures. The explosions make the leading front expand and curve considerably. Another characteristic of these flows is that the contact discontinuities that emanate from the triple points roll-up and shed vortices in the wake of the leading front. These sheets detach from the front during triple-point collisions and are subsequently convected away from the front.

The computational domain for the simulations is a rectangle with dimensions $80 \times 10\ L_{1/2}$. The initial condition consists of a transversally perturbed, planar ZND wave, propagating in a quiescent medium. The resolution of the simulations was 20 points per $L_{1/2}$. Periodic conditions are imposed on the top and bottom boundaries and inflow conditions are imposed on the right-hand boundary. Finally, outflow conditions (zero normal gradients of the flow variables) are prescribed on the left-hand boundary. In order to save memory and computing time, the computations have been performed on a moving frame. This is achieved by assigning a (constant) negative velocity component for the two-phase mixture on the right-hand boundary along the direction of the flow. In order for the instabilities to grow, the ZND wave is allowed to propagate through 64 $L_{1/2}$ of pure gas during the initial stages of the simulation.

6.1. *Mixtures with reactive particles*

Results for *Case A* at $t^* = 48\ t_{1/2}$ are plotted in figure 20. (t^* represents time lapsed after the ZND wave reached the two-phase mixture). The results depict the establishment of a flow field that is symmetric with respect to the horizontal axis that passes through the tip of the leading-front. Both gaseous and solid reactants burn rapidly inside a thin zone that is attached to the front. The leading-front structure also contains two triple points with opposite transverse velocities. The triple points eventually collide, creating an explosion that forces the shock to curve and the gas to expand. As a result, two new triple points are formed, moving in opposite directions. In this particular case, triple point collisions occur periodically. The simulations showed that the whole structure of the leading front oscillates periodically with time, which means that this is a two-dimensional pulsating detonation. The periodic oscillation of the detonation wave enforces the symmetry of the flow field behind it. Establishment of pulsating two-phase detonations with such characteristics has been observed experimentally by Zhang & Gronig (1992).

The evolution of the vorticity field behind the front for this case is particularly interesting. Figure 21 contains contour plots of the magnitude of the vorticity field at $t^* = 54\ t_{1/2}$. This figure shows that vortices are shed by the contact discontinuities that emanate from the triple points of the front. The contact surfaces are, in fact, shear layers that become unstable and roll up. The particle volume fraction inside these layers is high. The particles, however, have time to burn completely and, therefore, their concentration at the rolled-up tails of the layers is zero. Figure 21 shows two systems of contact discontinuities. The first one consists of the shear layers that are still attached to the leading-front structure. The layers will detach during the next

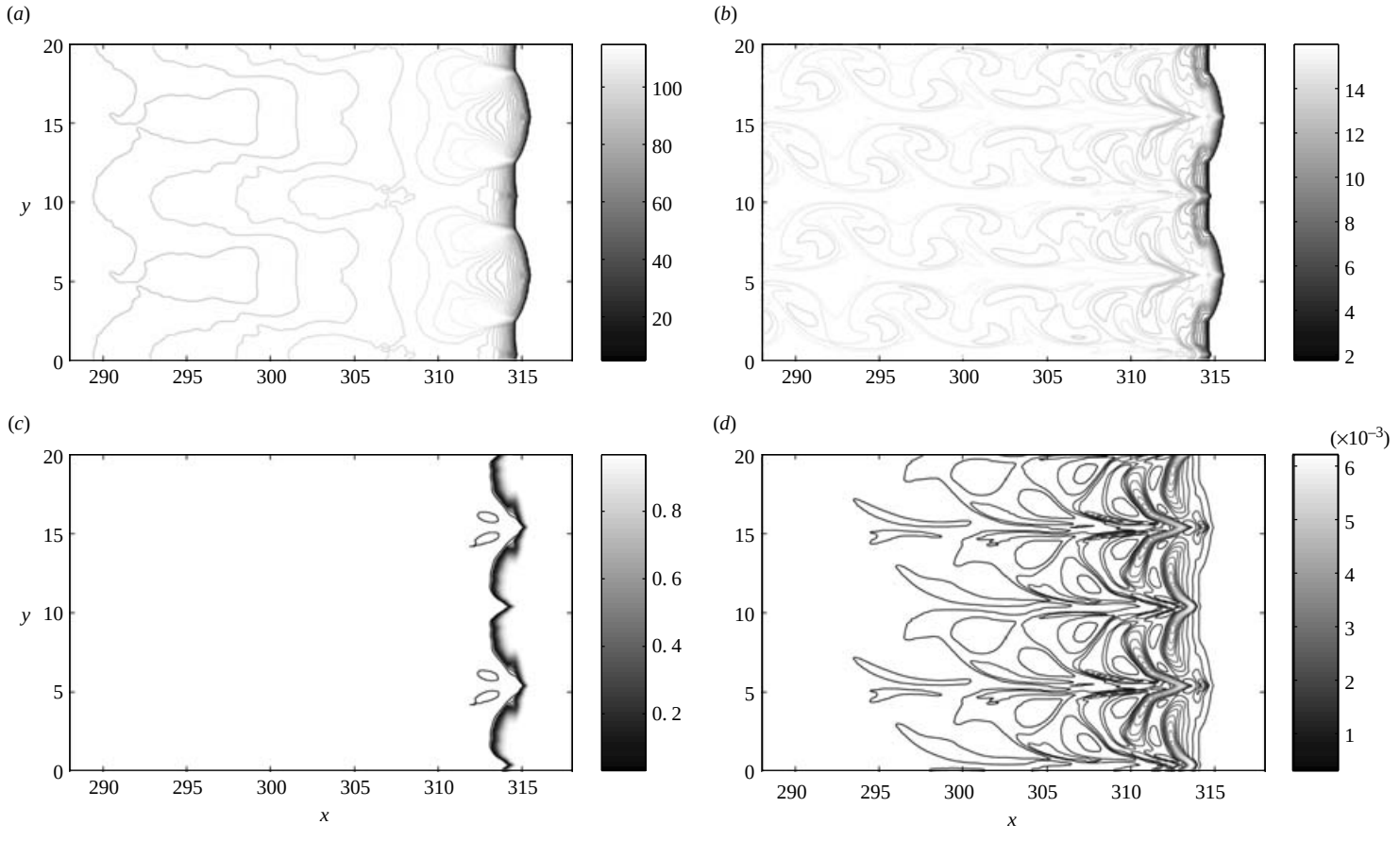

FIGURE 20. Case A, reactive particles. Flow variables at $t^* = 48\ t_{1/2}$. Two periods in the y-direction are plotted. (*a*) p_g. (*b*) T_g. (*c*) z. (*d*) ϕ.

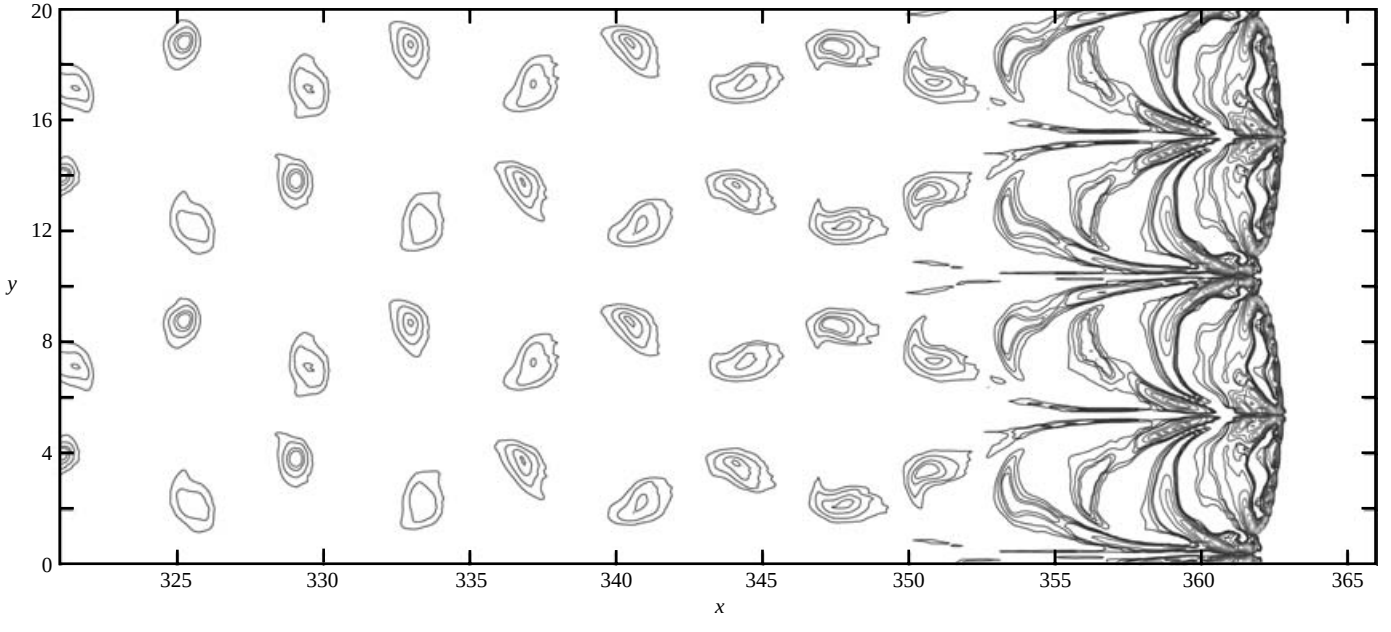

FIGURE 21. Case A, reactive particles. Magnitude of gaseous vorticity at $t^* = 54\, t_{1/2}$. Two periods in the y-direction are plotted.

triple-point collision. The second system consists of shear layers that detached in the previous collision and are located right behind the first system.

The flow field of this two-phase detonation is very similar to those computed for purely gaseous detonations with low activation energy and overdrives; see Bourlioux & Majda (1992), and Papalexandris *et al.* (2002). Those flows are also characterized by periodic oscillations of the front and symmetric flow-fields. On the other hand, the corresponding purely gaseous detonation (i.e. with the same gaseous reaction parameters) has a multitude of unstable modes and is characterized by strong reflected shocks and unburnt pockets of gas behind the main front.

Results for *Case B* are discussed next. The simulations show that the leading front remains planar even though triple points have already been formed. Apparently, the increased particle concentration of the mixture suppresses the transverse instabilities, just as in mixtures with inert particles. Numerical results for this case, taken at $t^* = 54\, t_{1/2}$, are plotted in figure 22. It is worth mentioning that in the previous section which dealt with one-dimensional flows it was predicted that the flow-fields of Cases A and B were very similar. This similarity, however, is not extended to two-dimensional flows because of the suppression of transverse instabilities that takes place in case B. Nonetheless, it is still possible that the instabilities grow substantially at a later time and produce a pulsating detonation similar to that developed in Case A.

An important characteristic of this case is that the detonation velocity is slightly higher than that predicted for case A, despite the substantial increase of ϕ_{s0}. By contrast, in one-dimensional simulations, it was predicted that higher particle volume fractions always result in lower detonation velocities. This phenomenon is apparently related to the lower growth rate of the instabilities and might not persist at later times.

Finally, we present results for the two-dimensional version of *Case C*. A sample of results, taken at $t^* = 54\, t_{1/2}$, are shown in figure 23. The plots show the development of two strong triple points on the leading front. The shear layers that originate at the triple points separate the domain behind the front into hot and cold regions. In the hot regions, the gases react very rapidly. By contrast, the gaseous reaction in the cold region proceeds slowly. At the same time, there is enhanced mixing of cold and hot mixtures in the shear layers. As a result, large pockets of partially unreacted material are formed. Once the reaction inside these pockets comes to completion, pressure waves are emitted in all directions. Another interesting feature of this flow is that the pressure gradients in the transverse direction are very small. The reason for this 'one-dimensional' character of the pressure field is that triple-point collisions have not yet occurred. Hence, the shock has not obtained significant curvature, implying that shock pressure is almost constant across the front. By contrast, the temperature field has significant transverse gradients, induced by the presence of the shear layers.

6.2. *Mixtures with inert particles*

First, *Case A* was considered. It was predicted that the primary effect of the particle addition is to suppress the transverse instabilities at the leading front. Triple points are still formed along the front, but their strength is greatly reduced. As a result triple-point collisions occur much less often than in the equivalent purely gaseous detonation or the equivalent case with reactive particles. This contributes to the preservation of a leading-front profile which is almost planar, i.e. it has very small curvature. Further, the pressure behind the shock oscillates with time, just as in the

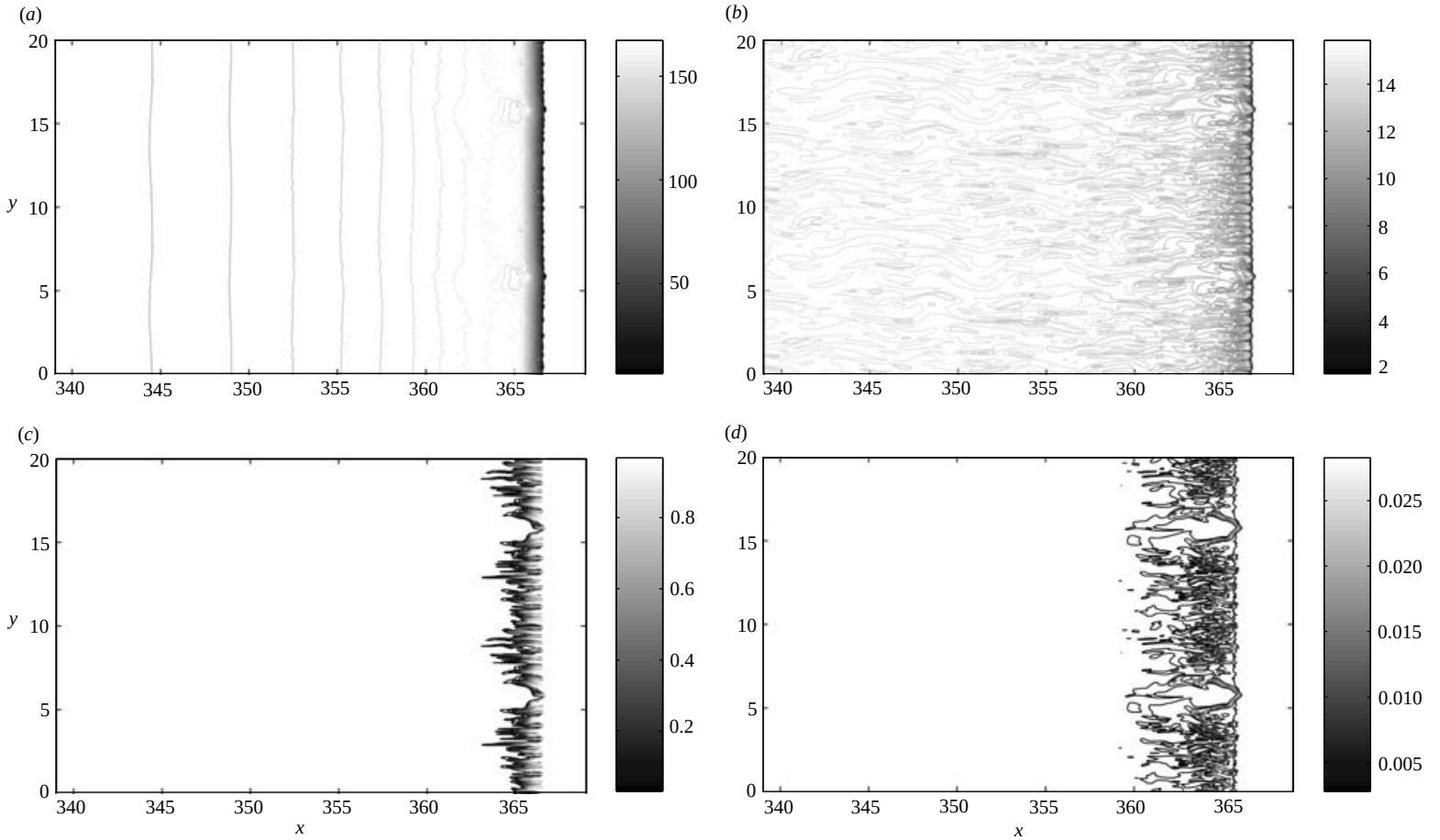

FIGURE 22. Case B, reactive particles. Flow variables at $t^* = 54\, t_{1/2}$. Two periods in the y-direction are plotted. (a) p_g. (b) T_g. (c) z. (d) ϕ.

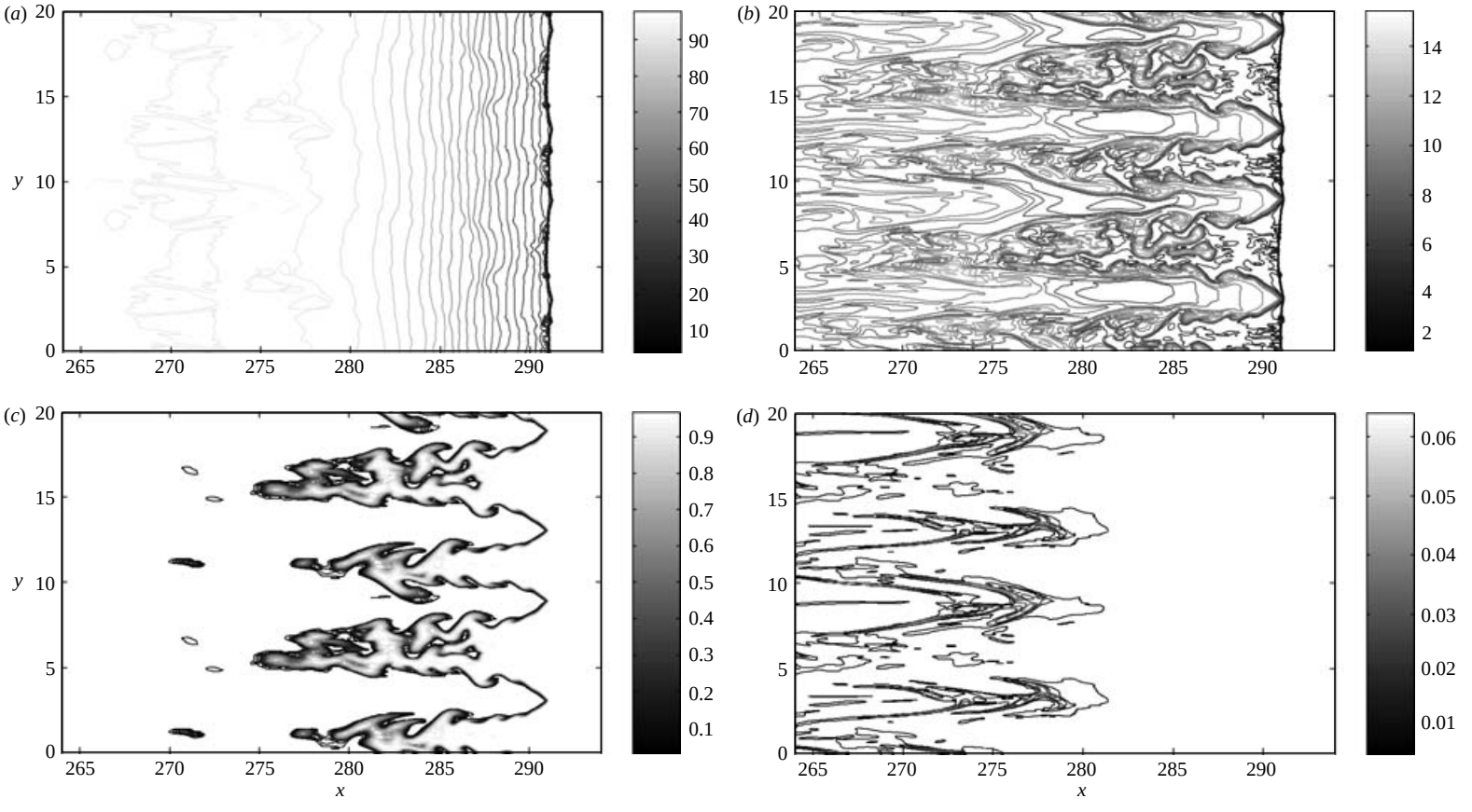

FIGURE 23. Case C, reactive particles. Flow variables at $t^* = 54\, t_{1/2}$. Two periods in the y-direction are plotted. (a) p_g. (b) T_g. (c) z. (d) ϕ.

corresponding one-dimensional case. Plots of the simulation for this particular case have not been included herein for brevity.

There is significant transversal variation of the reaction rate even though the curvature of the front is very small. This is a direct consequence of the triple-point formation that occurs along the leading front. In fact, the flow instabilities might be suppressed owing to the presence of particles, but they are not removed completely. Consequently, the flow adjusts itself via the triple-point mechanism. Part of the triple-point structure is a contact discontinuity. It separates material with different temperatures and different volume fractions in reactive gas. The numerical results further predict reaction zones that are longer than those in the corresponding one-dimensional case. This is due to increased strain resulting from the multi-dimensionality of the flow.

Numerical results of *Case B* are discussed next. Samples of these results, taken at $t^* = 55\, t_{1/2}$, are plotted in figure 24. In this case, the leading shock has curved because of the flow instabilities. The point of the shock with the highest curvature has been the centre of a triple point collision (and subsequent explosion) at an earlier time. However, even for this case, triple-point collisions are not as strong as in purely gaseous detonations; this suggests instability suppression by the solid particles. The planar parts of the leading front are characterized by lower temperatures (with respect to points with significant shock curvature), implying a slow-down of the reaction progress. As a result, an induction zone is formed behind the planar parts of the leading front. Inside this zone, the reaction is sustained due to thermal runaway.

Finally, results from the two-dimensional version of *Case C* are discussed. It was predicted once again that the pressure behind the leading front is almost constant along the transverse direction, and relatively low. Yet, formation and collisions between (much weaker) triple points still occur. The burning of the material begins in the vicinity of the explosion that follows such collisions. Elsewhere behind the front the material remains almost unreacted. Therefore, particularly long induction zones are formed. These zones eventually detach from the structure of the front, thus forming large pockets of unreacted material. Once the temperature inside these pockets reaches a certain threshold, the gas will react rapidly generating pressure waves that will interact with the main front. Plots of the simulation for this particular case have not been included herein for brevity.

Grid convergence studies for the cases presented above have also been performed. It was observed that the differences in the numerically predicted evolution of the detonations and the resulting flow fields decrease with successive grid refinements. Also, the numerical predictions for certain global parameters (such as wave speeds, time required for triple-point formation, etc.) showed small sensitivity on the grid size. However, it should be pointed out that in cases with many unstable modes, such as those presently examined, it is not realistic to expect point-to-point agreement between results from different resolutions.

We conclude our discussion with some general remarks regarding the two-dimensional simulations for two-phase detonations in mixtures with inert particles. These simulations show that the addition of inert particles in a combustible gas always reduces the detonation velocity and the burning rate of the gas, but it also suppresses the instabilities of the leading front. Further, higher initial particle volume fractions and/or smaller particle diameters decelerate the detonation and can eventually quench it.

The predicted dependence of the flow fields on the particle volume fraction and diameter agree qualitatively with the conclusions of the computational study of Loth *et al.*

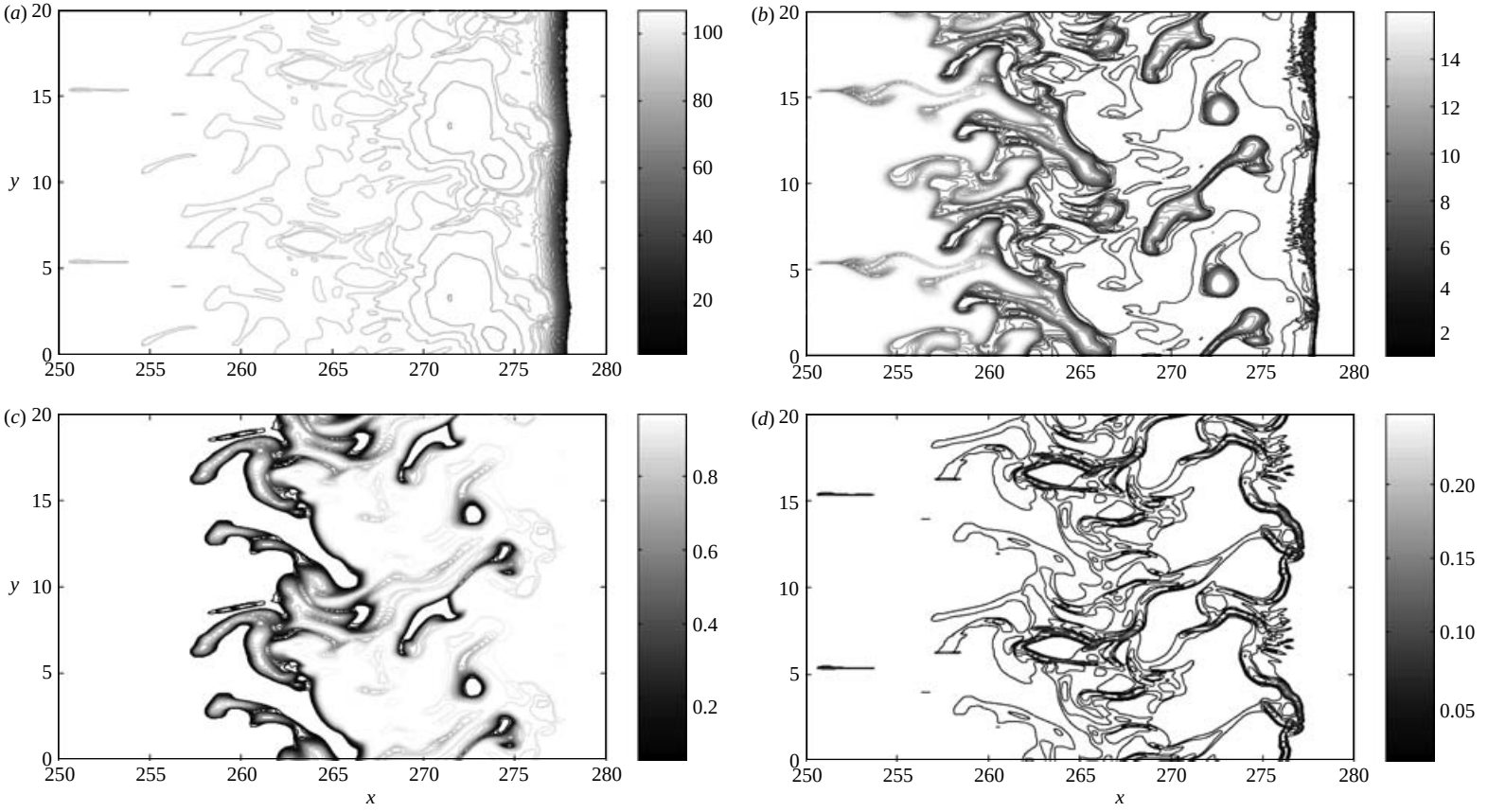

FIGURE 24. Case B, inert particles. Flow variables at $t^* = 55\ t_{1/2}$. Two periods in the y-direction are plotted. (a) p_g. (b) T_g. (c) z. (d) ϕ.

(1997), as well as the earlier experimental study of Lafitte & Bouche (1959). Both of these investigations concluded that the detonation velocity is more sensitive to ϕ_{s0} than to d_p and that sufficiently high ϕ_{s0} or d_p results in detonation failure. (By contrast, the experimental results of Kaufmann *et al.* (1984) imply that the detonations velocity is more sensitive to the particle diameter than to the volume fraction.) It is also worth mentioning that the computed detonation structures are quite similar to those predicted by Loth *et al.* (1997). More detailed comparisons cannot be made owing to the differences in the flow models and the boundary conditions.

7. Concluding remarks

In this paper, the structure of detonations in mixtures of gases and solid particles was examined numerically. The two-phase-flow model is based on the Eulerian description of motion for both phases. The particles, in particular, are described as an incompressible continuum. The model takes into account the volume occupied by the particles, but it does not include terms for the modelling of compaction dynamics phenomena. Further, it employs a simplified one-step reaction mechanism for both cases. The governing equations form a system of hyperbolic conservation laws with source terms which is solved numerically with a new unsplit solver. Algorithm validation was performed via numerical convergence studies, comparisons with reference solutions, and (whenever possible) comparisons with previous experimental results.

Numerical simulations for both one-dimensional and two-dimensional detonations were performed. It was predicted that the heat released by the particle burning suppresses the instabilities of the leading front, while the momentum and energy transfer from the gas to the particles results in lower detonation velocities and longer reaction zones. Regarding the one-dimensional simulations of two-phase detonations with reactive particles, the simulations predicted that the shock speed drops monotonically with the particle volume fraction. Sufficiently high volume fractions can cause detonation quenching. It was also confirmed that high particle diameters reduce the velocity of the front because they lower the burning rate of the particles.

Further, the simulations predicted the existence of three possible modes of propagation, as observed in earlier studies. In the first mode, the single-front detonation, the front is supported by heat release from both gaseous and solid phase reactions. This is the mode with the highest propagation speed. In the second and third modes (double-front, and pseudo-gas detonation, respectively), the front is supported by the heat from the gaseous reaction only. Our studies further indicated that steady-wave solutions are attainable for the first mode of propagation only.

The one-dimensional simulations for mixtures with inert particles predicted that, owing to the absence of mass transfer between the two phases, the length of the compaction zone increases with time. The detonation velocity drops rapidly with ϕ_{s0}. Sufficiently large particle volume fractions result in detonation failure. When such failure occurs, the reaction zone propagates with a velocity that is lower than that of the compaction zone, provided that the gaseous flow is subsonic (with respect to the laboratory frame) at the end of the reaction zone. Also, the detonation velocity increases slowly with increasing particle diameter, owing to lower drag and heat conduction between the two phases. Therefore, the effect of the particle diameter is different from that in mixtures with reactive particles. It was further confirmed

that the stability of the front is also influenced by the particle volume fraction and particle diameter. Higher values of ϕ_{s0} and lower values of d_p enhance the detonation stability.

Two-dimensional simulations provided further evidence for the stabilizing effect of reactive solid particles. The improved stability characteristics of such flows suggest that the injection of small heavy particles in the combustion chambers of detonation-based propulsion concepts might be a viable alternative for performance enhancement. Certain initial conditions resulted in pulsating detonations, characterized by periodic variation of the geometry of the front and symmetrical flow-fields. Other initial conditions resulted in detonations with an almost planar leading front. In these cases, the transverse pressure gradients are very small. The shear layers that emanate from the front are considerably prolonged and consist of relatively cold, partially reacted mixtures.

Two-dimensional simulations for mixtures with inert particles also predicted the suppression of the transverse instabilities which leads to smaller shock curvatures. The mechanisms of triple-point formation and collision, commonly encountered in purely gaseous flows, are still present, but the time scales associated with them are much larger. Occasionally, triple-point collisions lead to the formation of jets consisting of cold partially reacted gas and large numbers of particles. Such jets have not been observed in purely gaseous detonations.

These simulations showed that larger solid volume fractions do not always decelerate the detonation wave (see comparisons between the flow-fields of Cases A and B with reactive particles). This means that conclusions from one-dimensional simulations cannot always be applied to multidimensional flows. A consequence of this constraint is, among others, that calibration of simplified chemistry models from one-dimensional simulations might not be possible. Experiments with particle volume fractions at the levels considered in the present study, although desirable, are still difficult to perform for technical reasons, namely, difficulty in achieving uniformity of the two-phase mixture for sufficient time.

The author wishes to thank Professor A. Leonard of the California Institute of Technology for many fruitful discussions. He also wishes to thank the anonymous referees of this paper for providing comments and suggestions which led to significant improvements of the original manuscript.

Appendix

In this Appendix, we give the expressions for the convective velocities, $\hat{\boldsymbol{u}}_i$, $i = 1, \ldots, 10$ that appear in the expressions, (33), of the vector fields of the manifolds that are defined via (34). As mentioned in § 3, these velocities are introduced in order to decompose the governing system (7)–(8) into a set of o.d.e.s. For each o.d.e., there is a family of velocities that satisfies the decomposition (34). Each velocity corresponds to a different path on the manifold where the particular o.d.e. is valid.

For computational purposes, we have selected the velocities with minimal norm. Their expressions are:

$$\hat{\boldsymbol{u}}_1 = -\frac{G_4 - c^2 G_1}{|\nabla \tilde{p}_g - c^2 \nabla \tilde{\rho}_g|}\, \boldsymbol{N}_1, \qquad \boldsymbol{N}_1 = \frac{\nabla \tilde{p}_g - c^2 \nabla \tilde{\rho}_g}{|\nabla \tilde{p}_g - c^2 \nabla \tilde{\rho}_g|}, \tag{A1}$$

$$\hat{\boldsymbol{u}}_2 = -\frac{\Omega_1}{|\nabla \tilde{p}_g + \tilde{\rho}_g c \boldsymbol{n} \cdot \nabla \boldsymbol{u}_g|}\, \boldsymbol{N}_2, \qquad \boldsymbol{N}_2 = \frac{\nabla \tilde{p}_g + \tilde{\rho}_g c \boldsymbol{n} \cdot \nabla \boldsymbol{u}_g}{|\nabla \tilde{p}_g + \tilde{\rho}_g c \boldsymbol{n} \cdot \nabla \boldsymbol{u}_g|}, \tag{A2}$$

$$\hat{\boldsymbol{u}}_3 = -\frac{\Omega_2}{|\nabla \tilde{p}_g - \tilde{\rho}_g c \boldsymbol{n}\cdot\nabla \boldsymbol{u}_g|}\,\boldsymbol{N}_3, \qquad \boldsymbol{N}_3 = \frac{\nabla \tilde{p}_g - \tilde{\rho}_g c \boldsymbol{n}\cdot\nabla \boldsymbol{u}_g}{|\nabla \tilde{p}_g - \tilde{\rho}_g c \boldsymbol{n}\cdot\nabla \boldsymbol{u}_g|}, \tag{A3}$$

$$\hat{\boldsymbol{u}}_4 = -\frac{\left((G_2,\, G_3) - \tilde{\rho}_g^{-1}\nabla \tilde{p}_g\right)\cdot \boldsymbol{n}^{\perp}}{|\boldsymbol{u}_g \cdot \boldsymbol{n}^{\perp}|}\,\boldsymbol{N}_4, \quad \boldsymbol{N}_4 = \frac{\nabla(\boldsymbol{u}_g \cdot \boldsymbol{n}^{\perp})}{|\nabla(\boldsymbol{u}_g \cdot \boldsymbol{n}^{\perp})|}, \tag{A4}$$

$$\hat{\boldsymbol{u}}_5 = -\frac{G_5}{|\nabla z|}\,\boldsymbol{N}_5, \qquad \boldsymbol{N}_5 = \frac{\nabla z}{|\nabla z|}, \tag{A5}$$

$$\hat{\boldsymbol{u}}_6 = \frac{\phi_s \nabla\cdot u_s - G_6}{|\nabla \phi_s|}\,\boldsymbol{N}_6, \qquad \boldsymbol{N}_6 = \frac{\nabla \phi_s}{|\nabla \phi_s|}, \tag{A6}$$

$$\hat{\boldsymbol{u}}_7 = -\frac{G_7}{|\nabla u_s|}\,\boldsymbol{N}_7, \qquad \boldsymbol{N}_7 = \frac{\nabla u_s}{|\nabla u_s|}, \tag{A7}$$

$$\hat{\boldsymbol{u}}_8 = -\frac{G_8}{|\nabla v_s|}\,\boldsymbol{N}_8, \qquad \boldsymbol{N}_8 = \frac{\nabla v_s}{|\nabla v_s|}, \tag{A8}$$

$$\hat{\boldsymbol{u}}_9 = -\frac{G_9}{|\nabla T_s|}\,\boldsymbol{N}_9, \qquad \boldsymbol{N}_9 = \frac{\nabla T_s}{|\nabla T_s|}, \tag{A9}$$

$$\hat{\boldsymbol{u}}_{10} = \frac{N_s \nabla\cdot u_s}{|\nabla N_s|}\,\boldsymbol{N}_{10}, \qquad \boldsymbol{N}_{10} = \frac{\nabla N_s}{|\nabla N_s|}. \tag{A10}$$

In (A1)–(A10) c is the frozen speed of sound for the gaseous phase,

$$c = \sqrt{\frac{\gamma \tilde{p}_g}{\tilde{\rho}_g}}, \tag{A11}$$

while $\boldsymbol{n}$ is the unit vector normal on the cell interface, and $\boldsymbol{n}^{\perp}$ is the unit vector normal to $\boldsymbol{n}$. The algorithm, however, allows $\boldsymbol{n}$ to be an arbitrary but fixed spatial unit vector. Also, $G_i,\ i = 1, \ldots, 9$, are the source terms of the governing equations written in primitive form. In other words,

$$G_1 = \Gamma, \tag{A12}$$

$$G_2 = \frac{F_x + \Gamma(u_s - u_g)}{\tilde{\rho}_g}, \tag{A13}$$

$$G_3 = \frac{F_y + \Gamma(v_s - v_g)}{\tilde{\rho}_g}, \tag{A14}$$

$$G_4 = (\gamma - 1)\left(\boldsymbol{F}\cdot(\boldsymbol{u}_s - \boldsymbol{u}_g) + Q - q_1 R + \Gamma(c_s T_s + q2 + \tfrac{1}{2}|\boldsymbol{u}_s - \boldsymbol{u}_g|^2)\right), \tag{A15}$$

$$G_5 = \frac{R - z\Gamma}{\tilde{\rho}_g}, \tag{A16}$$

$$G_6 = -\frac{\Gamma}{\tilde{\rho}_s}, \tag{A17}$$

$$G_7 = -\frac{F_x}{\tilde{\rho}_s}, \tag{A18}$$

$$G_8 = -\frac{F_y}{\tilde{\rho}_s}, \tag{A19}$$

$$G_9 = -\frac{Q}{c_s \tilde{\rho}_s}. \tag{A20}$$

Finally, the terms $\Omega_{1,2}$ are given by

$$\Omega_{1,2} = \gamma \tilde{p}_g (\boldsymbol{n} \cdot (\nabla \boldsymbol{u}_g) \boldsymbol{n} - \nabla \cdot \boldsymbol{u}_g) + G_4 \pm \tilde{\rho}_g a (G_2, G_3) \cdot \boldsymbol{n}. \tag{A21}$$

REFERENCES

Afanasieva, E. A. & Levin, V. A. 1983 Multifront combustion of two-phase medium. *AIAA Prog. Astronaut. Aeronaut.* **87**, 394–413.

Baer, M. R. & Nunziato, J. W. 1986 A two-phase mixture theory for the deflagration-to-detonation transition (DDT) in reactive granular materials. *Intl J. Multiphase Flow*, **12**, 861–889.

Bdzil, J. B., Menikoff, R., Son, S. F., Kapila, A. K. & Stewart, D. S. 1999 Two-phase modeling of deflagration-to-detonation transition in granular materials: a critical examination of modeling issues. *Phys. Fluids* **11**, 378–492.

Bourlioux, A. & Majda, A. J. 1992 Theoretical and numerical structure for unstable two-dimensional detonations. *Combust. Flame* **90**, 211–229.

Bourlioux, A., Majda, A. J. & Roytburd, V. 1991 Theoretical and numerical structure for unstable one-dimensional detonations. *SIAM J. Appl. Maths* **51**, 303–343.

Butler, P. B. & Krier, H. 1986 Analysis of deflagration-to-detonation transition in high-energy solid propellants. *Combust. Flame* **63**, 31–48.

Cambier, J. L. & Bogdanoff, D. W. 1993 RAM acceleration from a two-phase detonative system. *Proc. First Intl RAMAC Workshop*, St Louis, France.

Chapman, S. & Cowling, T. G. 1961 *The Mathematical Theory of Non-uniform Gases.* Cambridge University Press.

Clavin, P., He, L. & Williams, F. A. 1997 Multi–dimensional stability analysis of overdriven gaseous detonations. *Phys. Fluids* **9**, 3764–3785.

Eidelman, S. & Yang, X. 1993 Detonation wave propagation in combustible particle/air micture with varaible particle density distributions. *Combust. Sci. Technol.* **89**, 201–218.

Erpenbeck, J. J. 1964 Stability of idealized one-reaction detonations. *Phys. Fluids* **7**, 684–696.

Fan, B. C. & Sichel, M. 1988 A comprehensive model for the structure of dust detonations. *Twenty-second Symp. (Intl) on Combustion*, pp. 1741–1750. The Combustion Institute, Pittsburgh, PA.

Gonthier, K. A., Menikoff, R., Son, S. F. & Asay, B. W. 1998 Modeling compaction-induced energy dissipation of granular HMX. *Eleventh (Intl) Symp. Detonation.* Snowmass, CO, USA.

Gonthier, K. A. & Powers, J. M. 2000 A high resolution numerical method for a two-phase model of deflagration-to-detonation transition. *J. Comput. Phys.* **163**, 1376–443.

Hwang, P., Fedkiw, R. P., Merriman, B., Aslam, T. D., Karagozian, A. R. & Osher, S. J. 2000 Numerical resolution of pulsating detonation waves. *Combust. Theor. Model.* **4**, 217–240.

Ishii, R.,Umeda, Y. & Yuhi, M. 1989 Numerical analysis of gas-particle two-phase flows. *J. Fluid Mech.* **203**, 475–515.

Kapila, A. K., Menikoff, R., Bdzil, J. B., Son, S. F. & Stewart, D. S. 2001 Two-phase modeling of deflagration-to-detonation transition in granular materials: reduced equations. *Phys. Fluids* **13**, 3002–3024.

Kaufmann, C. W., Wolanski, P., Arisoy, A., Adams, P. R., Maker, B. N. & Nicholls, J. A. 1984 Dust, hybrid, and dysty detonations. *AIAA Prog. Astronaut. Aeronaut.* **94**, 221–239.

Khaisanov, B. A. & Veyssiere, B. 1996 Initiation of detonation regimes in hybrid two-phase mixtures. *Shock Waves* **6**, 9–15.

Knudsen, J. G. & Katz, D. L. 1955 *Fluid Mechanics and Heat Transfer.* McGraw-Hill.

Laffitte, P. & Bouche, R. 1959 Suppression of explosion waves in gaseous mixtures by means of fine powders. *Seventh Symp. (Intl) on Combustion*, pp. 504–508. The Combustion Institute, Pittsburgh, PA.

Lee, H. I. & Stewart, D. S. 1990 Calculation of linear detonation instability: one-dimensional instability of plane detonation. *J. Fluid Mech.* **206**, 103–132.

van Leer, B. 1979 Towards the ultimate conservative difference scheme. V. A second order sequel to Godunov's method. *J. Comput. Phys.* **32**, 101–136.

Loth, E., Sivier, S. & Baum, J. 1997 Dusty detonation simulations with adaptive unstructured finite elements. *AIAA J.* **35**, 1018–1024.

Mamontov, G. M., Mitrofanov, V. V. & Sabbotin, V. A. 1980 Regimes of gaseous detonations in rigid porous medium. *Detonation. Chemical Physics of Combustion and Explosion Processes*, pp. 106–110. Chernogolovka (in Russian).

Miura, H. & Glass, I. I. 1982 On a dusty-gas shock tube. *Proc. R. Soc. Lond.* A **382**, 373–388.

Oran, E. S., Kailasanath, K. & Guirguis, R. H. 1988 Numerical simulations of the development and structure of detonations. *AIAA Prog. Aeronaut. Astronaut.* **114**, 155–170.

Papalexandris, M. V., Leonard, A. & Dimotakis, P. E. 1997 Unsplit schemes for hyperbolic conservation laws with source terms in one space dimension. *J. Comput. Phys.* **134**, 31–61.

Papalexandris, M. V., Leonard, A. & Dimotakis, P. E 2002 Unsplit algorithms for multidimensional hyperbolic Systems of conservation laws with source terms. *Comput. Maths Applic.* **44**, 25–49.

Peraldi, O. & Veyssiere, B. 1986 Experimental study of detonations in starch particle suspensions with O_2/N_2, H_2/O_2, and C_2H_4/O_2 mixtures. *AIAA Prog. Astronaut. Aeronaut.* **106**, 490–504.

Powers, J. M., Stewart, D. S. & Krier, H. 1990*a* Theory of two-phase detonations – Part I: modeling. *Combust. Flame* **80**, 264–279.

Powers, J. M., Stewart, D. S. & Krier, H. 1990*b* Theory of two-phase detonations – Part II, structure. *Combust. Flame* **80**, 280–303.

Rowe, P. N. 1961 Drag forces in a hydraulic model for fluidized bed. Part II. *Trans. Inst. Chem. Engng* **48**, 175–180.

Saint-Cloud, J. P., Guerraud, C., Moreau, M. & Manson, N. 1976 Experience sur la propagation des détonations dans un mileu diphasique. *Acta Astronaut.* **3**, 781–794.

Saurel, R. 1996 Numerical analysis of a RAM accelerator employing two-phase combustion. *J. Prop. Power* **12**, 708–717.

Saurel, R. & Abgrall, R. 1999 A multiphase Godunov method for compressible multifluid and multiphase flows. *J. Comput. Phys.* **150**, 425–467.

Saurel, R., Daniel, E. & Loraud, J. C. 1994 Two-phase flows: second-order schemes and boundary conditions. *AIAA J.* **32**, 1214–1221.

Saurel, R. & Lemetayer, O. 2001 A multiphase model for compressible flows with interfaces, shocks, detonation waves and cavitation, *J. Fluid Mech.* **431**, 239–271.

Sivier, S., Loth E. & Baum, J. 1996 Two-phase compressible flow simulations with unstructured adaptive finite elements. *AIAA J.* **34**, 1078–1080.

Smirnov, N. N., Zverev, N. I. & Tyurnikov, M. V. 1996 Two-phase flow behind a shock wave with phase transitions and chemical reaction. *Exp. Thermal Fluid Sci.* **13**, 11–20.

Tomboulides, A. G. & Orzag, S. A. 2000 Numerical investigation of transitional and weak turbulent flow past a sphere, *J. Fluid Mech.* **416**, 45–73.

Uphoff, U., Hanel, D. & Roth, P. 1995 Influence of reactive particles on the formation of a one-dimensional detonation wave. *Combust. Sci. Technol.* **110–111**, 419–441.

Veyssiere, B. 1986 Structure of detonations in gaseous mixtures containing aluminum particles in suspension. *AIAA Prog. Astronaut. Aeronaut.* **106**, 522–544.

Veyssiere, B., Arfi, P. & Khaisanov, B. A. 1999 Detonations of starch suspension in gaseous O_2/N_2 and stoichiometric H_2/O_2 mixtures. *Combust. Flame* **117**, 477–492.

Veyssiere, B. & Manson, N. 1982 Sur l'existence d'un second front de détonation des mélanges biphasiques hydrogène–oxygène–azote–particules d'aluminium. *C. R. Acad. Sci.* **295**, 335–338.

Wolinski, M., Kapuscinski, M. & Wolanski, P. 1995 Detonation processes in dusty mixtures of different oxygen contents. *AIAA Prog. Astronaut. Aeronaut.* **154**, 135–147.

Yao, J. & Stewart, D. S. 1996 On the dynamics of multi-dimensional detonations. *J. Fluid Mech.* **309**, 225–275.

Zhang, F. & Gronig, H. 1991*a* Transition to detonation in corn starch dust-oxygen and dust-air mixtures. *Combust. Flame* **86**, 21–32.

Zhang, F. & Gronig, H. 1991*b* Spin detonation in reactive particles oxidizing gas flow. *Phys. Fluids* A **3**, 1983–1990.

Zhang, F. & Gronig, H. 1992 Two-headed detonation in reactive particle–oxidizing gas-flow. *Phys. Fluids* A **4**, 2308–2315.